Hydrogeological characterization of alpine karst using the transient analysis of flow and transport

Sara Lilley[1,2] and Masaki Hayashi[1]

[1]Department of Earth, Energy, and Environment, University of Calgary, Calgary, Alberta, T2N 1N4, Canada

5 [2]BGC Engineering Inc., Calgary, Alberta, T2P 3L8, Canada

Correspondence to: Masaki Hayashi (hayashi@ucalgary.ca)

Abstract. Karst springs in alpine catchments are important for maintaining groundwater-dependent ecosystems in fragile environments and for sustaining baseflow in mountain rivers. Despite its importance, rugged and inaccessible terrains pose major challenges in hydrogeological studies of alpine karst. This study developed a practical approach for characterizing an
10 alpine karst system in the Canadian Rocky Mountains that had no previous information aside from the location of the spring outlet. Using geological maps, satellite images, simple water balance, water sampling and analysis, and dye tracer tests, it was possible to estimate the extent of the spring catchment and infer the hydrogeological characteristics of the karst system. Of particular importance was the information obtained from the fluctuations of spring discharge and electrical conductivity in response to diurnal snowmelt cycles. Synthesis of the diverse data set indicates that the karst system has a large volume of
15 groundwater stored in the fractured rock matrix that buffers the interannual variability of precipitation and sustains steady baseflow throughout the year. The karst system consists of fractured rock matrix, saturated conduits acting like pipes, unsaturated conduits acting like open channels, and many pools delaying the propagation of transport and hydraulic signals through the conduit network. The approach developed in this study will be applicable to other alpine karst systems in snow-dominated catchments in rugged and inaccessible terrains.

1 Introduction

Karst aquifers cover 15 % of the Earth's ice-free continental surface (Goldscheider et al., 2020) and supply freshwater to 9% of the global population (Stevanović, 2019). Karst aquifers in alpine terrains have distinct hydrogeological
25 characteristics, whereby high topographic gradients and lack of vegetative cover enhance groundwater circulation, and result in rapid recharge and highly seasonal flow (Werner, 1979). Springs discharging from karst aquifers sustain perennial flow in alpine streams and maintain stable water temperature, thereby providing an important ecological niche in fragile environments (Goldscheider, 2019; Stevanović et al., 2024, p.130). Despite their importance, research on alpine karst aquifers is limited due to difficulties of conducting hydrogeological field work in remote and rugged terrains. Previous
30 studies have been primarily conducted in the European Alps (e.g., Chen et al., 2017; Gremaud et al., 2009; Krainer et al., 2021; Schäffer et al., 2020). Most hydrogeological studies of alpine karst in North America were conducted in the Canadian Rockies from the 1970s to 1990s (e.g., Drake and Ford, 1976; Ford, 1971a, 1971b, 1983a, 1983b; Smart, 1983; Smart and Ford, 1986; Worthington, 1991), with only a few recent studies conducted in the United States (Lachmar et al., 2021; Tobin and Schwartz, 2020).

35 While the lack of vehicle access in remote alpine terrains pose major challenges for conventional hydrogeological field work, the unique alpine settings offer potential advantages that are not available in lowlands. Snow accumulation and melt has a strong hydrological influence in mid-latitude alpine regions, where the terrain is covered by snow for more than half of a year and rapid snowmelt over two to three months dominates the water input. This results in a binary mode of spring discharge consisting of a relatively short and intense freshet followed by a long period of baseflow. Snowmelt and glacier
40 melt have a pronounced diel cycle influencing the water input, resulting in strong diel fluctuations in discharge and water chemistry of alpine streams (e.g., Muir et al., 2011). The strong seasonal variability and diel fluctuations of water input may

be transmitted from recharge areas to the spring through the complex flow pathways consisting of fractured rock matrix and conduits (e.g., Worthington et al., 2016). The modulation of input 'signals' along the flow pathways may be interpreted using standard signal-analysis methods, offering valuable insights into the hydrogeological behaviour of the karst system.

45   The signal-analysis approach (e.g., cross-correlation analysis) has been commonly used in karst hydrogeology (Fiorillo and Doglioni, 2010; Howell et al., 2019; Jódar et al., 2020; Kovacic, 2010; Mangin, 1984; Rahnemaei et al., 2005), however, their application to diel signals in snowmelt-dominated systems has not been widely explored.

In this study, a previously unstudied alpine karst spring in the Canadian Rockies is used to develop a practical approach for the hydrogeological characterization of alpine karst systems in remote, rugged terrains. The research objectives are: (1)

50   delineate the extent of the spring catchment, (2) evaluate the relative volume of groundwater stored over winter with respect to seasonal discharge during the high flow period, (3) characterize the flow and transport dynamics of the karst system, and (4) develop a set of tools for hydrogeological investigation of similar alpine karst systems. The insights and tools developed in this study will be useful for characterizing similar mountain karst systems in snow-dominated regions and their responses to changes in environmental conditions.

55

2 Study Site

This study investigated the hydrogeology of the Watridge Karst Spring (WKS), located on the northern tip of Mount Shark (50° 50' 36" N, 115° 25' 38" W) at an elevation of 1870 m (Figure 1). The adjoining Spray Mountains are

60   approximately 30-km long and consist of steep-sided mountain ridges and glaciated alpine cirques. Treeline occurs at approximately 2300 m, above which the ground is mostly barren as the growing season is too short for tree growth (Downing and Pettapiece, 2006). The mountain ridges continue south to Mount Sir Douglas (3406 m). The spring outlet is situated on a shady north-facing slope, accessible only by foot on a 5-km hiking trail. The spring provides year-round humidity to the surrounding forest, creating a unique habitat for hygrophytic shrubs and mosses (Toop and de la Cruz,

65   2002). Twenty-five species of mosses, eight hepatics, and seven lichens were identified by WCBLIG (2015), highlighting the uniqueness of the spring's microclimate providing moist habitats. The relatively large entrance and high volume of water discharging from the spring holds promise for an extensive cave network (Lilley and Crisp, 2022).

Although the source of spring water had not been identified prior to the current study, the WKS is expected to be recharged by snowmelt and rain over the rugged terrain of northern Spray Mountain range. The high-elevation snowpack

70   can persist until August, and the upper sections of glaciers are perennially covered in snow. The mean annual air temperature at the Burstall Pass automatic weather station (AWS) (Figure 1) was −0.5°C during 2014–2023 (CRHO, 2025), while the mean annual precipitation was 1183 mm. During 2017–2023, mean annual discharge of the WKS was $1.9×10^7$ m^3 y^{-1} (or 600 L s^{-1}), varying between 16 and 3200 L s^{-1}, with the median value of 300 L s^{-1}.

The Front Range of the Rocky Mountains is dominated by major thrust faults, and both broad and steeply dipping folds

75   of Paleozoic and Mesozoic strata (McMechan, 2012). The bedrock of Spray Mountains is composed of the massive Palliser Fm., a major cliff-forming unit consisting primarily of limestone and dolomitic limestone (Holter, 1976; de Wit and McLaren, 1950). A stratal thickness of approximately 280 m is typical in the Front Ranges (de Wit and McLaren, 1950). The Palliser Fm. is an established karst unit in the Front Ranges (Smart, 1988; Yonge and Lowe, 2017) and is known to have groundwater velocities exceeding 0.1 m s^{-1} (Worthington, 1991). Anhydrite has been described as an important

80   constituent of the uppermost and lowermost sections of the Palliser Fm. (Andrichuk, 1960; Clark, 1949; Fox, 1951; Govett, 1961; MacNeil, 1943; Nightingale and Mayer 2012). The WKS occurs at the base of the Palliser Fm., at the inferred contact between the Palliser Fm. and the underlying Sassenach Fm. (McMechan, 2012; Lilley, 2023), which is considered an aquitard (Worthington, 1991). The Mississippian Exshaw and Banff Fms. overly the Palliser Fm. These units are composed

of black pyritiferous shales, interbedded mudstones, limestones, siltstones, and sandstones; and they do not behave as karst

85   aquifers (Beales, 1956; McMechan, 2012).
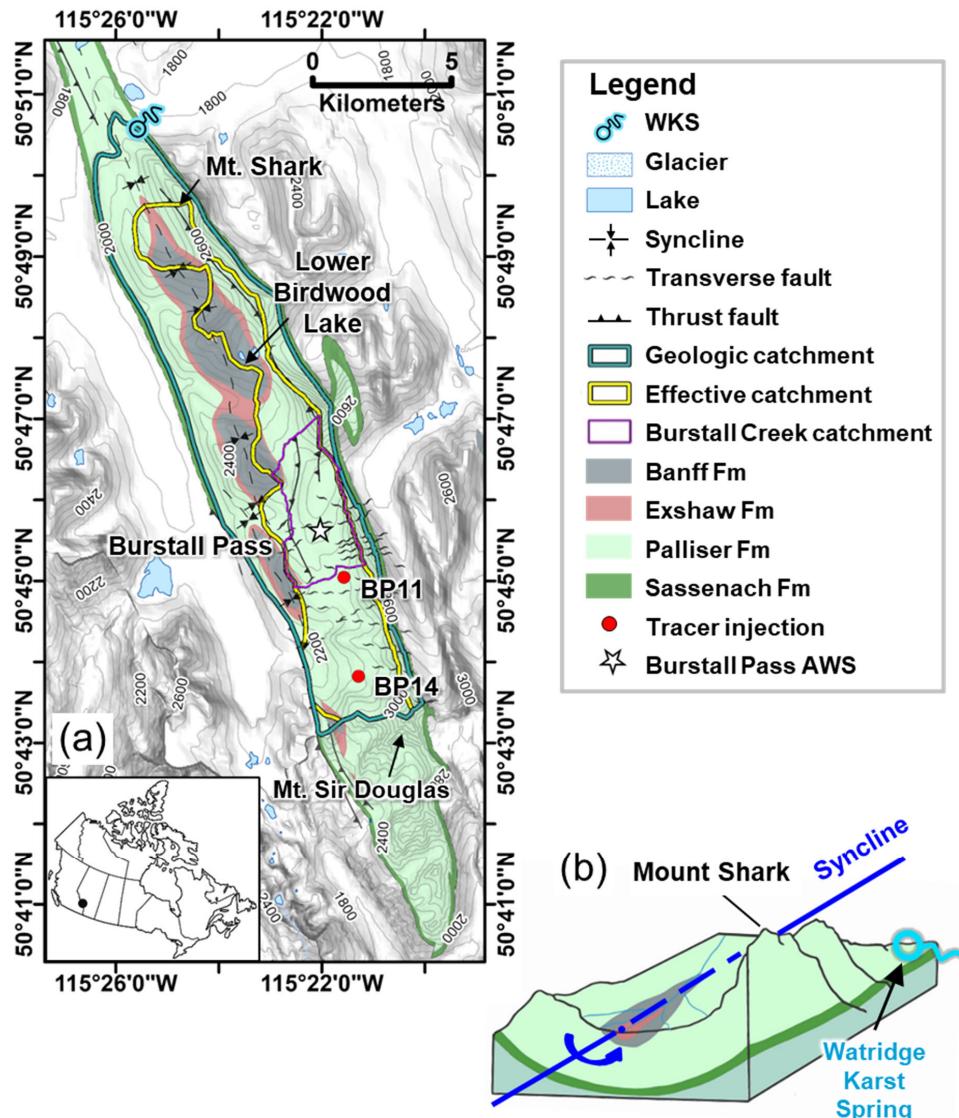
Figure 1 (a) Map of the northern Spray Mountains showing relevant geological formations within a regional plunging syncline, trending NNW-SSE. Elevation contour lines (100 m interval) are drawn to indicate topography. The map also shows the extent of hydrological features and tracer release points. The insert shows the location of the study site within Canada. (b) A conceptual block diagram showing the structure of the plunging syncline with respect to the summit of Mount Shark, and the Watridge Karst Spring (WKS). The colours correspond to the geological formations in the legend.

90   In the southern direction along the Spray Mountains, the continuous extension of the Palliser Fm. above the elevation

of the WKS is a potential recharge area. Surface karst geomorphology, sinking streams, depressions serving as infiltration

basins (Figure 2a) are prevalent in the plateau area south of Burstall Pass AWS and towards Mount Sir Douglas. Several

shafts, dolines, and limestone pavements were observed on the plateau. Snowmelt has been observed cascading into vertical shafts, and the influence of daily snowmelt is noticeable in diel fluctuations of discharge and electrical conductivity (EC) of

95   the WKS (see below). Lilley (2023) observed a low amount of total annual runoff (23 mm) in Burstall Creek draining a small (4.5 km²) watershed located within the plateau area (Figure 1a), indicating that much of runoff occurred as subsurface drainage to the karst system. Smaller but considerable amount of recharge is expected in other parts of the catchment devoid of vegetation. For example, Lilley (2023) estimated a recharge rate of 10 mm d⁻¹ from the Lower Birdwood Lake (Figure 1a) in a topographically closed basin during a 20-day period in September 2020, indicating the ability of the weathered near-

100   surface zone of Banff Fm. to allow local infiltration of snowmelt water.
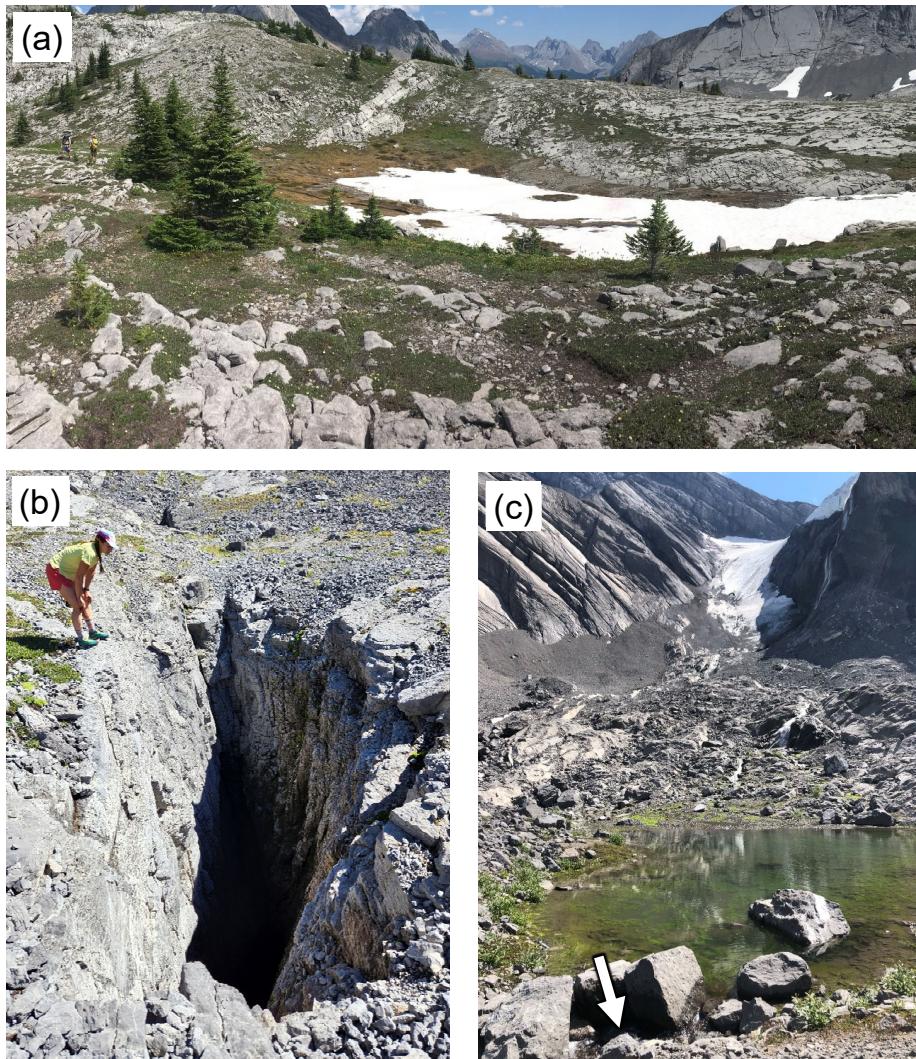
Figure 2 (a) Limestone pavement in foreground and a depression serving as a natural infiltration basin in the Burstall plateau near BP11 (9 July 2021). (b) Tracer injection location (BP11) in dry condition (31 August 2022). (c) Pond draining into a swallet (arrow), which served as a tracer injection location (BP14); looking south towards Mount Sir Douglas (11 Augst 2021).

3 Methods

105

3.1 Stream discharge and physical parameters

The WKS was continuously monitored from 2017 to 2023. Water level was recorded at 30-minute intervals using a non-vented pressure transducer (Solinst, Levelogger) in a stilling well and compensated for barometric pressure measured using a separate transducer (Solinst Barologger) located approximately 5 m from the spring outlet. Stream discharge was

110 manually measured using the velocity-area method (Dingman, 2002, p. 609) and a horizontal-axis current meter (Global Water, FP111) on a regular basis. Sources of uncertainty in the stream hydrographs are manual discharge measurement errors, curve fitting errors, and the accuracy of the recorder. Hood et al. (2006) found that the coefficient of variability for an alpine stream discharge measured by the same method was up to 9 %. Regular discharge measurements across the full spectrum of flow conditions minimized the uncertainty for the WKS hydrograph. A root-mean-squared error (RMSE) of 85

115 L s^{-1} was obtained for the WKS rating curve from 43 measurements of stream discharge, yielding an uncertainty of 13 %. Assuming that individual error components are independent and randomly distributed, the total uncertainty of the WKS hydrograph is ~16 % (Rosenberry and Hayashi, 2013, p.171).

Data loggers were used to record EC and water temperature and were calibrated using manual measurements. EC was measured using a handheld meter (VWR, 21800-012) and compensated to 25°C (Hayashi, 2004). EC was recorded at 30-

120 minute intervals using a conductivity sensor (Onset HOBO, U24-001) at an accuracy of ±5 μS cm^{-1} and was automatically compensated to 25°C. Manual EC measurements served to correct for instrumental drift of the logger. Water temperature was recorded by a platinum resistance temperature detector built into a pressure transducer (Solinst, Levelogger) at 30-minute intervals, with an accuracy of ±0.05 °C. Temperature readings were checked against manual measurements using a handheld thermocouple thermometer (Omega Engineering, HH-25TC).

125

3.2 Spring water sampling and analysis

A total of 125 spring water samples were collected and analyzed for major ion chemistry. All samples were filtered with a 0.45-μm membrane filters and stored in a refrigerator in pre-rinsed high-density polyethylene bottles prior to analysis. During May–October of 2020 and 2021, samples were collected every 1 to 4 days by an autosampler (Teledyne ISCO, 6712)

130 at the WKS. To minimize evaporation, each sample bottle contained a ping-pong ball and was filled to the narrow portion of the bottleneck so that the ball covered most of the water surface.

Major cations and anions were measured using ion chromatography (Metrohm 930 Compact IC Flex) with an analytical precision of 0.2 to 0.8 %. Alkalinity was determined by titration with an estimated uncertainty of 3 %. Samples with a charge balance error > 5 % were rejected. The ^{2}H/^{1}H and ^{18}O/^{16}O isotopic ratios of water were measured by a cavity ring-down

135 spectroscopy (Los Gatos Research, DLT-100) and reported as δ-values relative to the Vienna Standard Mean Ocean Water (V-SMOW) with an analytical uncertainty of 0.1 ‰ for δ^{18}O and 1 ‰ for δ^{2}H. Tritium in water was analyzed at the University of Waterloo Environmental Isotope Laboratory using liquid scintillation counting after 15-times enrichment by electrolysis, providing a detection limit of 0.8 tritium units (TU).

Select samples from the spring were analyzed for stable isotope ratios of dissolved SO$_4$ (^{34}S/^{32}S and ^{18}O/^{16}O). The

140 samples were processed following the standard SO$_4$ extraction technique (Lilley, 2023) and the isotope ratios of dissolved SO$_4$ were analyzed using continuous flow-isotope ratio mass spectrometry. The isotope ratios are reported as δ-values relative to Vienna Canyon Diablo Troilite for ^{34}S and the V-SMOW for ^{18}O with an analytical uncertainty of 0.3 ‰ for δ^{34}S and 1 ‰ for δ^{18}O.

Water samples for dissolved ^{222}Rn were collected from the spring in two 250-mL glass bottles by submerging them

145 underwater in the spring and the cap was fastened while underwater to prevent contamination from atmospheric gases. The ^{222}Rn activity was measured in the laboratory with a portable radon detector (Durridge, RAD7). A closed-loop aeration

device (Durridge, RAD H2O) was used, whereby air recirculated through the water sample to continuously extract radon until a state of equilibrium is achieved. The ^{222}Rn activity in water was calculated by multiplying the air loop concentration by a fixed conversion coefficient dependent on the sample size using CAPTURE software (Durridge Company Inc., 2014)
150   and corrected for the decay during storage.

3.3 Meteorological data

Air temperature and precipitation data recorded at the Burstall Pass AWS (Figure 1) were used in this study. The AWS is in an open canopy forest just below treeline at an elevation of 2260 m (CRHO, 2025), and the instruments include an air
155   temperature/relative humidity sensor (FTS, SDI-THS-LB) and a weighing precipitation gauge (OTT, Pluvio²). Precipitation data were supplemented by the data from nearby weather stations (ACIS, 2025; CRHO, 2025) to fill short gaps. Consistency across data sources was ensured through double mass curve analysis, which also helped detect any discrepancies across precipitation records. In cases of potentially erroneous precipitation data, historical radar data extracted from ECCC (2025) was consulted to verify the occurrence, timing, and extent of a precipitation event. Due to these gap-filling measures, it was
160   not practical to apply the correction for wind-induced undercatch of solid precipitation for the entire data set. Therefore, the precipitation data were used without correction. The magnitude of undercatch is estimated to be ~5 % of annual precipitation (Smith et al., 2022, Fig. 6b).

3.4 Fluorometry and dye tracing

165   A fluorescent dye tracer, uranine (colour index: Acid Yellow 73, CAS No. 518-47-8) was used in this study. Uranine has a low sorption tendency, low detection limit, low toxicity, and relatively conservative behaviour (Goldscheider et al., 2008). A fluorometer (Turner Designs, Cyclops 7F) was installed at the WKS, equipped with a shade cap, fastened to a steel-bar post that was hammered into the stream bed, and connected to a datalogger (Campbell Scientific, CR1000).

Three tracer injections were performed at two locations: BP11 and BP14 (Figure 1). Due to long hikes required to reach
170   the tracer injection locations, the dye was carried in powder form and dissolved in surface water from the local source. The BP11 site is a large shaft (Figure 2b) and is one example of many surface karst features on the Burstall Pass plateau. The entrance to BP11 is located at the base of a large (> 8000 m²) depression that holds snow until middle or late July. This snow drains into the shaft, making it a suitable location for tracer injection as the dye could be flushed by the melting snow. The BP14 site is a swallet that drains the glacial meltwater from the western glacier of Mount Sir Douglas (Figure 2c).

175   Tracer velocities and mean travel times were calculated from the resultant breakthrough curves. The mean travel time (t_m, s) is the time required for the centre of mass of the dye cloud to traverse the entire length of the aquifer system and defined by (USEPA, 2002):

$$t_m = \int_0^\infty tU(t)Q(t)dt \Big/ \int_0^\infty U(t)Q(t)dt \qquad (1)$$

where t (s) is the time elapsed since injection, U and Q are uranine concentration (kg m^{-3}) and spring discharge (m^3 s^{-1}) at
180   time t, respectively.

The mean tracer velocity (v_m, m s^{-1}) is given by (Mull et al., 1988; USEPA, 2002):

$$v_m = l_s / t_m \qquad (2)$$

where l_s (m) is an estimated length of the tracer travel path. A sinuosity factor (S_F) is used to estimate l_s from the linear distance l_{min} (m) between the injection and sampling points, reflecting a more realistic conduit path length (Field and Nash,
185   1997; Worthington, 1991, p. 138):

$$l_s = S_F l_{min} \qquad (3)$$

where typical values of S_F for solutional conduits range from 1.3 to 1.5 (USEPA, 2002). Worthington (1991) reported an average S_F of 1.56 for 96 complete flow paths in karst aquifers from around the world. Among these, the Castleguard karst in

the Front Ranges (Smart, 1983), 190 km northwest of the WKS had an S_F of 1.21. Based on these published figures, a range

190   of S_F from 1.2 to 1.6 was used in this study to estimate lower and upper bounds of groundwater velocities.

3.5 Analysis of diel fluctuations of discharge and EC

Spring discharge and EC had diel fluctuations in response to snowmelt and glacier melt as demonstrated in an example

of EC fluctuations (Figure 3a). To examine the effects of snowmelt on spring discharge and chemistry, air temperature was

195   used as a proxy for the magnitude of energy inputs for snowmelt. More specifically, it was assumed that, on a given day, the

timing of maximum snowmelt coincided with maximum air temperature, meaning that the daily peak of total energy input by

net radiation and turbulent heat transfer coincided with the peak air temperature and that the transit time of snowmelt

through the snowpack was of secondary importance. The time lag of diel fluctuations between air temperature and discharge

defined the hydraulic response time, and air temperature and EC the transport response time, analogous to pulse-through

200   time and flow-through time defined by Ford and Williams (2007, p.125).
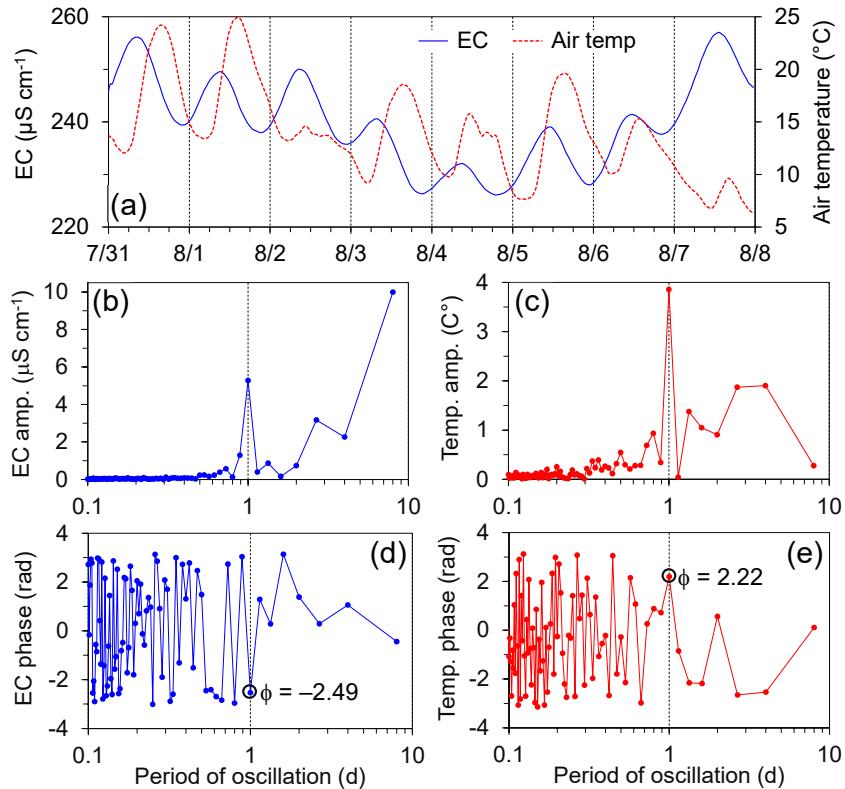
Figure 3 An example of fast Fourier transform (FFT) results from 31 July – 8 Augst 2021. (a) The original time series of electrical conductivity (EC) and air temperature. A four-hour moving average filter was applied to smooth the data for the plotting purpose. (b) Amplitudes of EC signal in the frequency domain plotted against the period of oscillation. (c) Amplitudes of air temperature in the frequency domain. (d) Phase angles (ϕ) of EC signals. (e) Phase angles of air temperature. The phase angles of the diel component are indicated in the graphs.

The Fourier transform was used to determine the phase hours (i.e. timing of peaks and troughs) of diel fluctuations, and

the phase hours of EC and discharge were compared against the phase hour of air temperature to determine the phase lag.

The fast Fourier transform (FFT) algorithm of Virtanen et al. (2020) was used to compute the discrete Fourier transform:

$$F_k = \sum_{n=0}^{N-1} f_n e^{-i2\pi kn/N} \tag{4}$$

where F_k is the kth element of the transformed sequence in the frequency domain, f_n is the nth element (i.e. data point) of the original time series, N is the total number of data points, k is the index of the frequency component in the frequency domain, ranging from 0 to N–1, and n is the index of the time-domain sequence.

The output of the FFT is an array of complex numbers F_k, which contains information on the timing (i.e. phase) and strength (i.e. amplitude) of each frequency in the original function. The phase and magnitude of diel signals were computed throughout the snowmelt season of 2020 and 2021 by (1) extracting an 8-day period from a given dataset (e.g., Figure 3a), (2) applying the FFT, and (3) shifting the period forward by two days and repeating the computation. Each 8-day data period was linearly detrended to allow for the periodic extension of the time series data.

Of particular interest is the diel component with an oscillation period (T_p) of 24 h, which has a corresponding angular frequency (= $2\pi / T_p$) of 0.2618 rad h⁻¹. The amplitudes of F_k plotted against T_p (Figures 3b and 3c) indicate the relative strength of oscillation in discharge (in L s⁻¹) or EC (μS cm⁻¹) contained in each component. For each 8-day period, the phase angle (ϕ, rad) of frequency components were computed from F_k (Figures 3d and 3e), and ϕ of the diel component was converted from radians to hours by multiplying ϕ by $T_p / 2\pi$. This provided a 'phase hour' as a time relative to 0000 hours (midnight). For example, a phase hour of +8.5 signified a signal maximum that occurred 8.5 h prior to midnight (i.e., 1530 hours) in Mountain Daylight Time (Coordinated Universal Time minus 6 hours). Conversely, a phase hour of –9.5 signified a maximum that occurred 9.5 h after midnight (i.e., 0930 hours). Finally, the difference between the phase of air temperature and EC/discharge was determined. This method provides a reliable means of determining phase lag, but with the inherent problem that results may represent any multiples of 24 h. To determine the actual time lag, visual inspection of EC/discharge to clearly defined events, such as a sudden stoppage or weakening of snowmelt due to cold weather (Figure 4), was used to calibrate the phase hours.
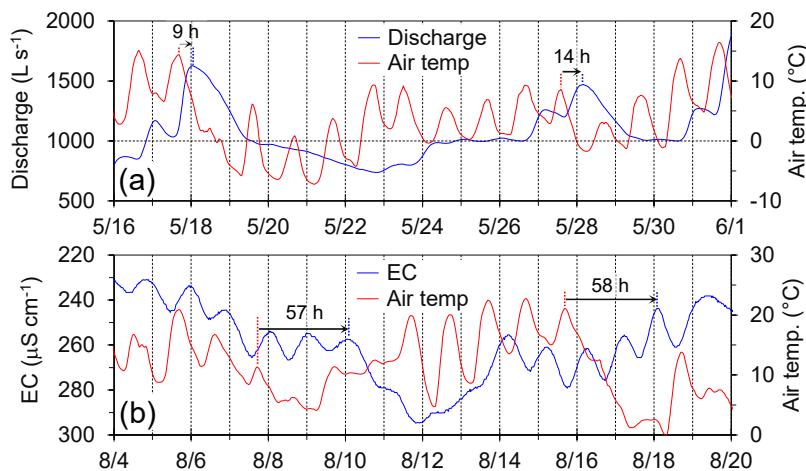
Figure 4 (a) Spring discharge and air temperature during 16 – 31 May 2021, indicating time lags between air-temperature and discharge peaks corresponding to snowmelt-stoppage events. Vertical lines indicate the midnight of each day. (b) Electrical conductivity (EC) and air temperature during 4-19 August 2021, indicating time lags between air-temperature peaks and EC troughs corresponding to weakening of snowmelt flux. Note that a reverse scale is used for EC.

4 Results

4.1 Dye tracer experiments

230

Each tracer test captured a complete break through curve (Figure 5a) demonstrating the connection between the tracer release points and the WKS. The tracer release at BP11 took place on 14 July 2022, during active snowmelt. The tracer was dissolved in snowmelt water and poured into the pit, where a visually estimated flow rate of 0.05 L s^{-1} was entering the shaft. Due to the scarcity of naturally flowing water, some dye losses were anticipated. The BP14(1) tracer test was

235 conducted on 17 September 2021, during a brief period of low air temperature (Figure 6a) that halted the flow of glacial meltwater into the swallet. Water from nearby puddles was used to dissolve the dye prior to injection and was followed by approximately 760 L of additional water in an attempt to flush the dye to the water table, and the cold period was followed by a warm storm event with 24 mm of rain in 30 hours (Figure 6a). The BP14(2) tracer test was conducted on 30 August 2022, while meltwater was actively draining into the swallet, allowing for immediate flushing of the dye, and potentially

240 reducing dye losses.
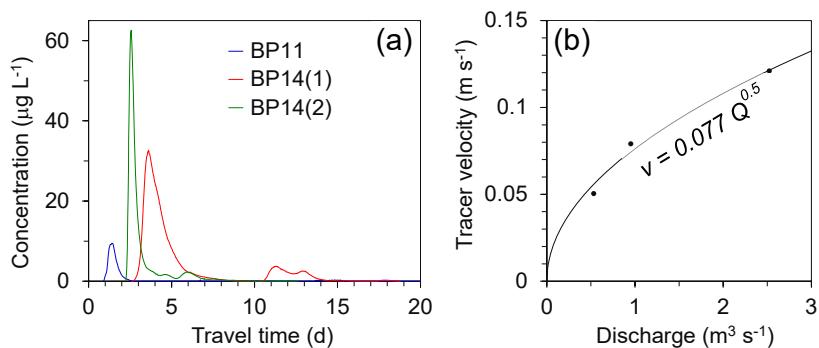
Figure 5 (a) Breakthrough curves for the three dye tracer tests. Estimated tracer concentration is plotted against the time since the tracer release to the conduit system. (b) Relation between spring discharge and mean tracer velocity during the three dye tracer experiments, calculated with a sinuosity factor (S_F) of 1.4. The solid line indicates a power function determined by the least-squares regression. The leading coefficient of the function changes to 0.070 and 0.093 when S_F = 1.2 and 1.6, respectively, are used.

Table 1 Summary of dye tracer tests: BP14(1), BP14(2), and BP11.

Parameter	Symbol	Unit	BP14(1)	BP14(2)	BP11
Linear distance to spring	l_{min}	km	13.7	13.7	11.2
Tracer travel path length[1]	l_s	km	16.4–20.6	16.4–20.6	13.4–16.8
Elevation		m	2445	2445	2463
Average spring discharge	Q_{av}	L s^{-1}	600	940	2300
Time to first arrival	t_1	day	2.6	2.2	0.9
Time to peak	t_p	day	3.6	2.5	1.4
Mean transit time	t_m	day	4.0	2.7	1.4
Mean tracer velocity[1]	v_m	m s^{-1}	0.048–0.063	0.071–0.094	0.11–0.15
Total mass of injection	M_{in}	kg	4.84	2.85	2.90
Apparent mass recovery[2]		%	57	115	43

[1]Upper and lower bounds represent a range of values corresponding to the expected range of sinuosity factor ($1.2 \leq S_F \leq 1.6$).
245 [2]Same fluorometer calibration coefficient is used for all tests, where actual coefficients likely differed between the tests.

A fluorometer calibration was conducted in the field on 22 April 2022 and yielded a calibration coefficient of 0.16 µg L^{-1} per mV. Laboratory calibrations were also attempted after completing all tracer tests, but gave inconsistent values of calibration coefficients. Due to these discrepancies, there is low confidence in the accuracy of the calibration coefficient, and

250   meaningful analysis of tracer data could only be conducted in a qualitative manner. Nevertheless, the coefficient determined
in the field test (see above) was used to convert the sensor mV output to tracer concentration, which were used to calculate
tracer travel time and velocities, adjusted for S_F ranging from 1.2 to 1.6 (Eq. 3). The breakthrough curves for BP14 tests had
secondary peaks (Figure 5a) suggesting that a small fraction of tracers may have traveled through multiple flow paths.

     Results of the three tracer tests are summarized in Table 1. Given that the tracer was released to actively flowing water
255   at an entrance of the conduit system in both BP14(2) and BP11 tests, the actual time of release was used to indicate the start
of these tests. For BP14(1), it was expected that the tracer was retained in the unsaturated part of the conduit system until a
heavy storm on the following day flushed it into the actively flowing conduit system. Therefore, the end of the storm event
was used to indicate the start of the test. This is reflected in the calculation of tracer travel time in Table 1. Tracer velocity
increased with average spring discharge during each test as expected (Figure 5b). The velocity appeared to be linearly related
260   to the square root of discharge, and a power function was used to estimate the transport velocity (v, m s^{-1}) of the system from
discharge Q (m^3 s^{-1}):

$$v = aQ^{0.5} \tag{5}$$

where a is an empirical coefficient taking a value of 0.082 m$^{-1/2}$ s$^{-1/2}$ for an intermediate value of S_F (= 1.4) within the
expected range.

265

4.2 Recharge area delineation

     The potential recharge area of the WKS was first delineated from the geological map strata (McMechan, 2012). The
area is geologically confined to the Palliser Fm. within a regional syncline, with the underlying Sassenach Fm. acting as an
aquitard. The area must extend to Mt. Sir Douglas based on the tracer test, giving a geologically possible extent of catchment
270   (36 km^2) indicated in Figure 1. However, not all the geologically defined area is expected to contribute meaningful amounts
of recharge. Snowmelt and rain on steep bedrock cliffs and slopes quickly becomes overland flow, which must be retained in
relatively flat areas, where it infiltrates rapidly into the karst system. Forested valley floors with perennial streams are
groundwater discharge areas and unlikely serve as effective recharge area. Using these as a guide, likely recharge area is
further constrained to 18 km^2 as indicated in Figure 1. This gives a rough estimate of the effective catchment of the WKS.
275   The feasibility of the catchment estimated above is evaluated using a simplified annual water balance:

$$A_C = V / [P - (ET + S) - R] \tag{6}$$

where A_C is the catchment area (m^2), V is the total volume of discharge at the WKS (m^3), P is precipitation (m), ET is
evapotranspiration (m), S is snow sublimation (m), and R is surface runoff (m). The average annual water balance was
calculated using the data from hydrological years 2017 to 2023, where a hydrological year is defined as 1 November – 31
280   October because snow accumulation usually starts in late October.

     Using the data from Burstall Pass AWS, P was estimated to be 1183 mm. Evapotranspiration and sublimation, while
not directly measured in this study, were estimated as follows. Direct measurement of ET and S in alpine catchments are
rare in the Canadian Rockies, but Hood and Hayashi (2015) examined the detailed water balance of an alpine catchment at
the Lake O'Hara study site located 80 km northwest of the WKS and determined average annual discharge of Opabin Creek
285   in 2007 and 2008 to be 1110 mm, whereas average annual precipitation was 1190 mm (He and Hayashi, 2019). The
difference is attributed to $ET + S$, and most of it is likely S because ET during the snow-free period (~ 3 months) from
mostly non-vegetated catchment is expected to be minimal. MacDonald et al. (2010) examined sublimation in an alpine sub-
catchment of the Marmot Creek basin located 20 km east of the WKS and estimated the mean annual sublimation in 2007
and 2008 to be 80 mm. These studies give a rough estimate of $ET + S$ as 80 mm. It is difficult to estimate R, but Lilley
290   (2023) estimated total annual runoff of ~20 mm in 2021 in Burstall Creek draining the central part of recharge area (Figure
1a). Using a rough estimate of 80 mm for $ET + S$ and 20 mm for R, Eq.6 gives $A_C \cong 17$ km^2, which is similar to the estimate

of 18 km^2 based on geology and topography. While these estimates have a large degree of uncertainty, A_C = 18 km^2 is used in the catchment water balance calculations in Section 4.8.

4.3 Seasonal dynamics of spring discharge, water temperature, and EC

The seasonal dynamics of spring discharge, water temperature, and EC were consistent between 2020 and 2021. Only the 2021 data are described here, while the 2020 data are shown in the electronic supplement (Figure A1). As air temperature rose in the Spray Mountains during April and May (Figure 6a), the rapid transmission of snowmelt from the catchment area was indicated by substantial increases in discharge of up to 1600 L s^{-1} during 15–18 May (Figure 6c). Decreases in both water temperature and EC indicated snowmelt dilution (Figure 6b and 6c). Diel fluctuations in discharge and EC (Figure 6d) caused by diurnal snowmelt were observed from the beginning of the snowmelt season until late September.

Noticeable changes in the behaviour of discharge and EC occurred around 18–23 July, when the magnitude of diel fluctuations of discharge decreased and that of EC increased (Figure 6d). As the discharge receded and dropped below 1000 L s^{-1}, the discharge recession slope flattened, and EC began rising towards stable winter levels. Therefore, this appears to define a transition point in the hydrochemical behaviour of the system, and hereafter referred to as the 'hydrochemical transition point'. A similar hydrochemical transition point was observed around 10–15 August 2020 at a discharge value of 1000 L s^{-1} (Figure A1).
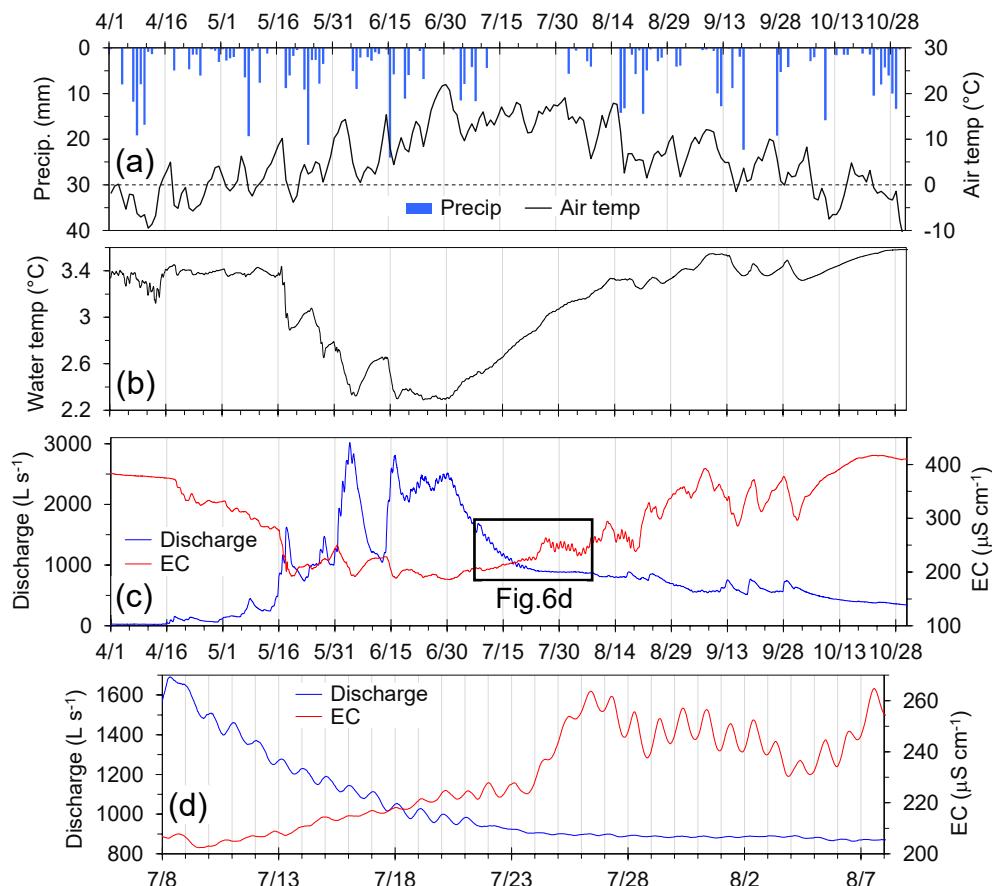
Figure 6 (a) Daily total precipitation and daily mean air temperature measured at the Burstall Pass weather station, 1 April – 31 October 2021. (b) Water temperature at the spring outlet. (c) (c) Spring discharge and electrical conductivity (EC). (d) Spring discharge and EC during 8 July – 8 August 2021.

4.4 Magnitude and phase of diel fluctuations

310   The magnitude of diel fluctuations of discharge and EC had distinct seasonal patterns (Figure 7b). The magnitude for discharge fluctuations was large during the high-flow period, equivalent of 3–9 % of the daily mean discharge, and decreased to less than 1 % of the mean discharge around the hydrochemical transition point of 18–23 July. In contrast, the magnitude of EC fluctuations was relatively small, equivalent of 1–2 % of the daily mean EC, and increased rapidly after the hydrochemical transition point, reaching a maximum of ~5 % of the daily mean EC.

315   Diel fluctuations of discharge had a phase delay of approximately 0.5 d compared to air temperature throughout the entire season (Figure 7c), meaning that the hydraulic response of the spring to diurnal snowmelt inputs was nearly constant. In contrast, the phase delay of EC gradually increased and reached ~3.5 d in September (Figure 7d), meaning that the transport response time of the spring became longer. The transport response time determined by the phase analysis was consistent with the result of the dye tracer test (Figure 7d). Note that the travel time of peak tracer concentration, not the

320   center of mass, is used in the figure. This is necessary because the phase lag is determined from the analysis of concentration data alone, not the product of concentration and discharge (i.e. mass flux).
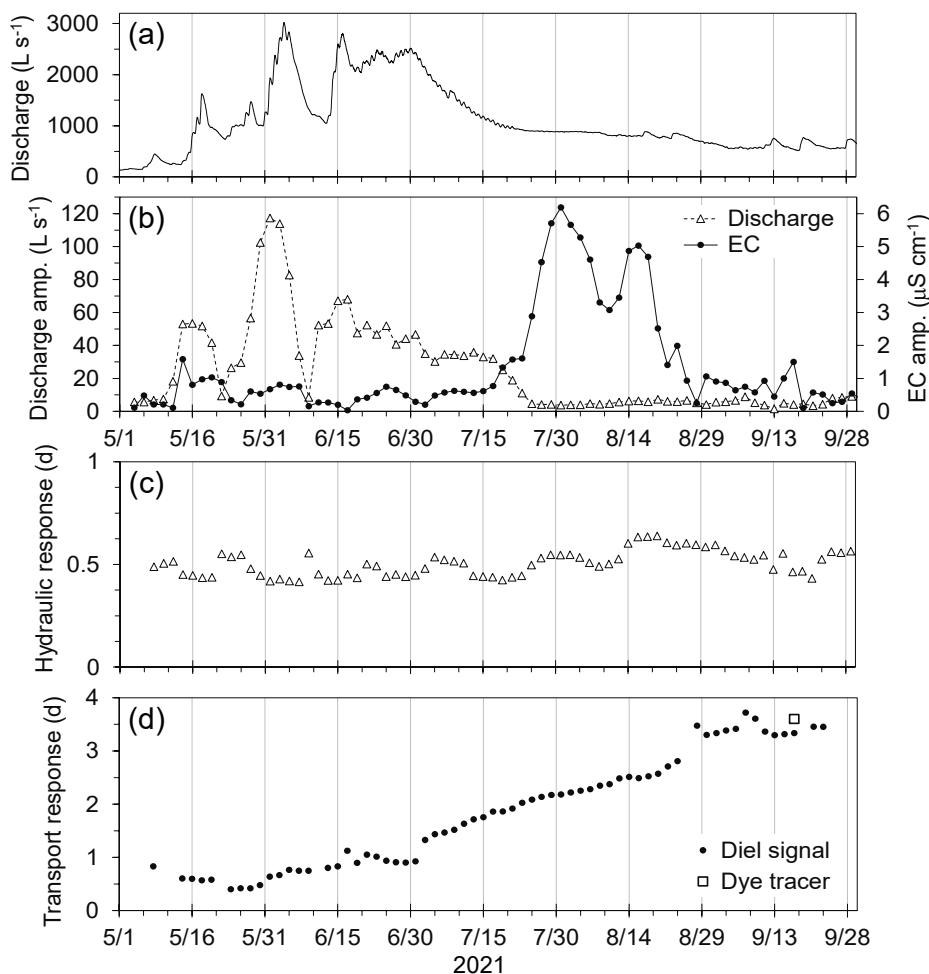
Figure 7 (a) Spring discharge during 1 May − 30 September 2021. (b) Amplitude of diel fluctuations of spring discharge and electrical conductivity (EC) during the same period. (c) Hydraulic response time of spring discharge determined by the analysis of diel fluctuations. (d) Transport response time of EC to diurnal snowmelt (i.e. diel signal) and the dye tracer travel time determined using the peak concentration arrival.

4.5 Chemical and isotopic composition

The chemical composition of all spring water samples was dominated by Ca and Mg (> 98% of total cations in meq L^{-1})

325   and alkalinity and SO$_4$ (> 99% of total anions). Since the pH of all samples ranged between 7.68 and 7.82, essentially all

alkalinity is attributed to HCO$_3^-$ (Domenico and Schwartz, 1998, p. 257). Therefore, concentrations of the four ions (Ca^{2+},

Mg^{2+}, HCO$_3^-$, and SO$_4^{2-}$) represent the hydrochemical dynamics of the spring. In general, concentrations of the four ions

decreased during the high-flow period due to dilution of over-winter storage with fresh snowmelt water (Figure 8a).

However, changes in concentration were asynchronous among the ions, resulting in different ratios of cations and anions

330   over the season.
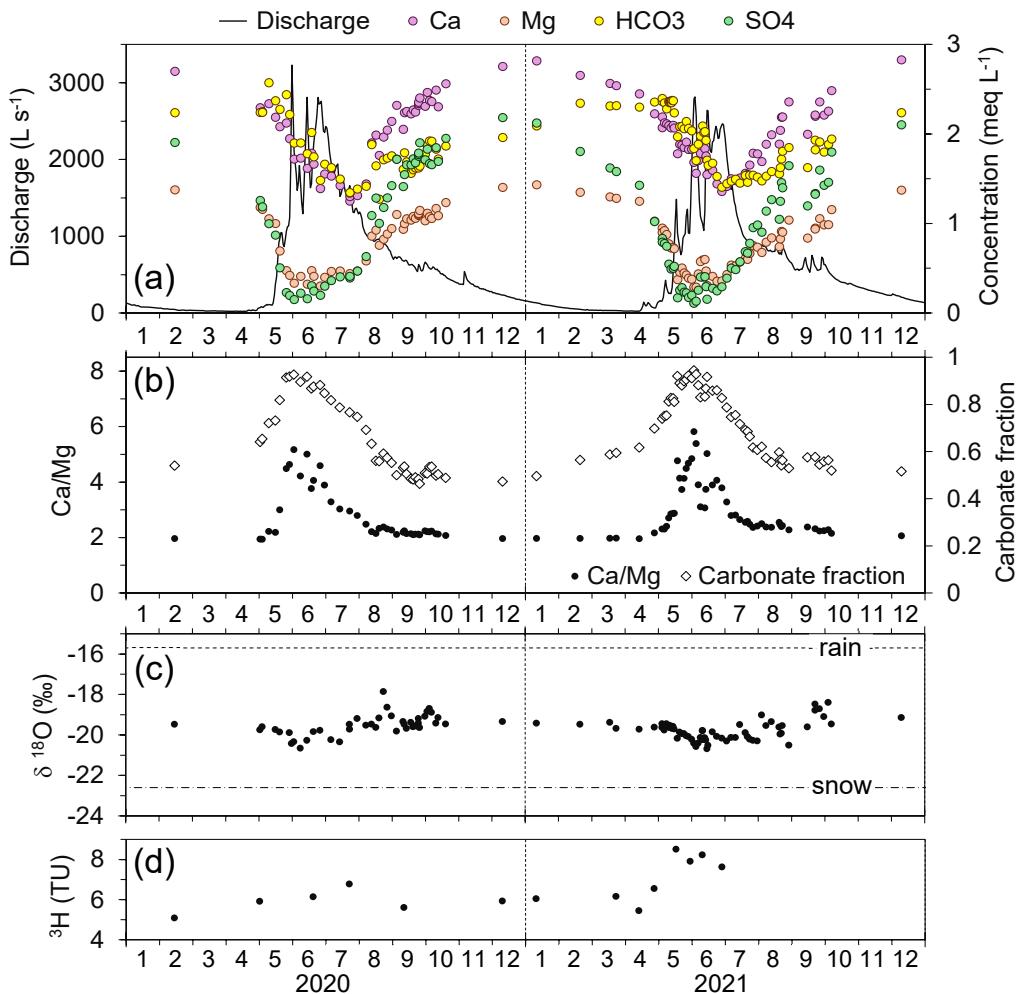
Figure 8 (a) Spring discharge and concentrations of dominant ions during January 2020 to December 2021. (b) The Ca-to-Mg ratio and carbonate fraction of spring water. (c) Oxygen stable isotope ratio of spring water. Horizontal lines indicate the mean isotope compositions of rain and snow samples. (d) Tritium content of spring water.

For example, the Ca/Mg concentration (meq L^{-1}) ratio became remarkably constant after the hydrochemical transition

point (mid-August in 2020 and mid-July in 2021) and remained constant until snowmelt (Figure 8b). The carbonate fraction,

[HCO$_3^-$] / ([HCO$_3^-$] + 2[SO$_4^{2-}$]), also had a distinct seasonal pattern (Figure 8b), where [ ] indicates molar concentration.

335   These suggest that there are at least two types of groundwater in the system: the over-winter component having a constant

Ca/Mg ratio (= 2) and relatively high ion concentration, and the component associated with snowmelt recharge having a

higher Ca/Mg ratio and carbonate fraction but lower ion concentrations. It is impossible to perform quantitative endmember mixing analysis of the two components because all four species are reactive, however, the information is useful for qualitative understanding of the groundwater system.

340   Based on the geologic setting (Figure 1a), the spring water likely derives its chemical contents from the minerals in the Palliser, Banff, and Exshaw Fms. through the dissolution of calcite, dolomite, anhydrite, and pyrite. A preliminary calculation shows that attributing all dissolved SO_4 to anhydrite ($CaSO_4$) does not leave enough Ca to account for the release of Mg from the dissolution of dolomite or magnesian calcite. Therefore, part of SO_4 must come from the dissolution of magnesium-sulfate minerals or the oxidation of pyrite. This will be examined further in the discussion.

345   Isotopic compositions of rain and snow samples plotted along a straight line (Figure A2) defining the local meteoric water line (LMWL) of: $\delta^2H = 7.55(\pm0.08) \times \delta^{18}O + 0.03(\pm1.54)$, where bracketed numbers indicate 95% confidence intervals. It was not possible to calculate volume-weighted mean compositions, but arithmetic mean compositions ($\delta^{18}O$, δ^2H) of all samples were (-15.7 ± 2.7, -119 ± 22) for rain and (-22.6 ± 1.2, -170 ± 9) for snow, where the uncertainty indicates one standard deviation. The spring water samples also plotted along the LMWL and had relatively small seasonal

350   variability, as demonstrated by $\delta^{18}O$ values shown in Figure 8c. They were mostly constrained between -20.5 and -18.5 ‰, and deviated only slightly from the average value of -19.7 ‰ during the high-flow periods, when the chemical compositions responded strongly to the influx of snowmelt recharge (Figure 8b). The difference between chemical and isotopic behaviours of spring water will be examined further in the discussion.

The spring water had moderately high tritium content indicating post-1950 recharge (Figure 8d). The values did not

355   have obvious seasonal pattern in 2020, but the tritium content appear to increase during the high-flow period in 2021. The nearest available long-term data of tritium in precipitation are from Ottawa, located ~3000 km east of the WKS (IAEA, 2025). The tritium content in precipitation during 1995–2019, corrected for radioactive decay (half life = 12.3 y) to January 2021, had substantial seasonal and inter-annual variability (Figure 9), and gradually increased from 3–10 TU in the late 1990s to 8–15 TU in recent years. It is impossible to determine the residence time of water, considering the possible

360   variability of tritium contents between Ottawa and the WKS, but in an approximate sense, it seems likely that most spring water samples had a residence time of five to ten years.
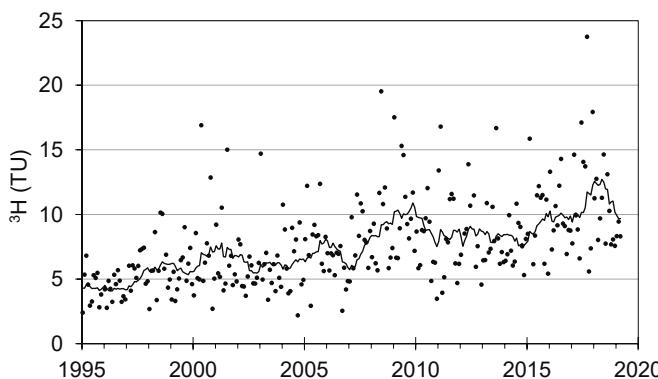
Figure 9 Tritium content in precipitation monitored in Ottawa, Canada (IAEA, 2025). The values are corrected for radioactive decay to January 2021. The line indicates backward 12-month moving average.

4.6 Dissolved radon activity

The activity of dissolved ^{222}Rn had a distinct seasonal pattern similar to discharge (Figure 10a), however, relatively

365   high ^{222}Rn activity (> 2 Bq L^{-1}) was sustained into early winter even after discharge decreased to low values (< 500 L s^{-1}). This is similar to seasonal patterns observed in cave systems in Switzerland (Eisenlohr and Surbeck, 1995) and Italy (Peano et al., 2011).

Carbonate minerals forming limestone and dolomite generate relatively little ^{222}Rn due to a lack of ^{226}Ra distributed on mineral surfaces (Eisenlohr and Surbeck, 1995). However, weathered fragments of Palliser limestone can generate sizable

370   ^{222}Rn inputs as indicated by a laboratory experiment using talus deposits consisting of Palliser limestone in a previous study (Christensen et al., 2020) at the Hathataga Creek catchment located ~16 km east of the WKS (Figure A4). The accumulation of ^{222}Rn in initially ^{222}Rn-free water is described by (Hoehn et al., 1992; also Appendix B):

$$A(t) = A_e \, [1 - \exp(-\lambda t)] \tag{7}$$

where $A(t)$ is the ^{222}Rn activity (Bq L^{-1}) at time t (d), A_e is the ^{222}Rn activity at steady state with ^{226}Ra, and λ is the

375   radioactive decay constant of ^{222}Rn (= 0.18 d^{-1}). Equation 7 indicates that the infiltrating water (i.e. recharge flux) needs to reside in ^{226}Ra-containing soil or weathered rock for 13 days to reach $A(t) > 0.9A_e$ if the material is completely saturated, and much longer if the material contains some air. This gives a qualitative constraint on the minimum transit time of snowmelt or rainwater before it enters the karst conduit network.
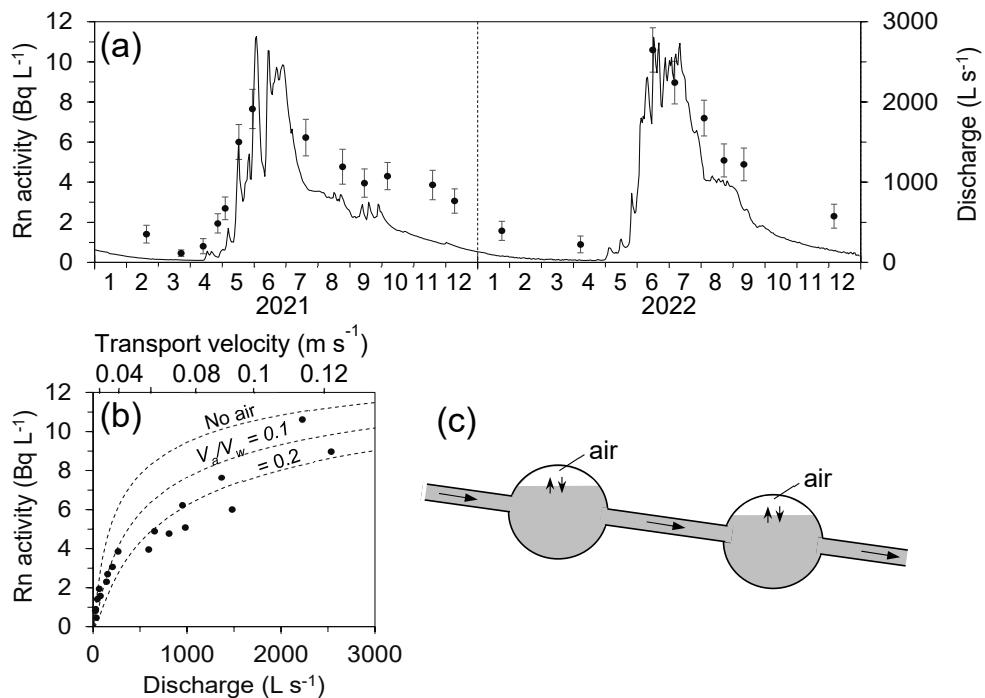
Figure 10 (a) Spring discharge and the activity of dissolved ^{222}Rn in spring water. Error bars indicate the analytical uncertainty. (b) Relation between spring discharge and ^{222}Rn activity. Dashed line indicates the theoretical decay curve for the initial activity of 15 Bq L^{-1} for cases with no air in the system, and air-to-water volume ratio (V_a/V_w) of 0.1 and 0.2. The top horizontal axis shows transport velocity calculated from discharge using Eq. 5. (c) Conceptual model of ^{222}Rn transport in the karst system consisting of water-saturated conduits and partially air-filled chambers, where the air-water exchange of ^{222}Rn takes place.

380   Once the water is in the conduit network, where little addition of ^{222}Rn occurs due to low ratio of rock surface area to water volume (Appendix B), dissolved ^{222}Rn undergoes exponential decay with a half life of ~3.8 d. Therefore, longer transit time in the conduit network will result in lower ^{222}Rn activity. Using the discharge-velocity relation estimated from the tracer tests (Eq. 5) and assuming a linear distance of 12 km between the recharge area and the spring and $S_F = 1.4$, theoretical ^{222}Rn activities at the spring for different discharge values are shown in Figure 10b (line labeled 'No air'). An initial ^{222}Rn activity

385   of 15 Bq L^{-1} is used in the calculation, based on the values observed at a non-karst spring discharging from a moraine aquifer containing Palliser limestone at Hathataga Creek, where an approximate residence time of groundwater was determined to be

50–100 d using a dye tracer (He and Hayashi, 2023). The observed ^{222}Rn activities plot far below the no-air line at low to medium discharge suggesting additional loss of ^{222}Rn by degassing.

Radon has a relatively high Henry's law constant of $N_a/N_w \approx 4.5$, where N_a and N_w are molar concentrations in air and water, respectively (SRNL, 2017). To gain qualitative understanding of the effects of degassing, an analysis is performed using a simple transport model in water-air system consisting of water-saturated conduits and partially air-filled chambers (Figure 10c). Air and water phases are in equilibrium with respect to ^{222}Rn activity while dissolved ^{222}Rn travels at a constant velocity. The equilibrium assumption is justified considering a rapid air-water exchange rate of dissolved ^{222}Rn (Peano et al., 2011). In a field experiment on 29 June 2021, a water sample collected ~30 m downstream of the outlet spring had only ~20 % of ^{222}Rn activity compared to the samples collected at the spring, indicating substantial degassing over a short distance. The transport and decay of ^{222}Rn in a moving packet of water (i.e. Lagrangian transport) is described by:

$$\frac{dA}{dt} = -\lambda\left(1 + H_c\frac{V_a}{V_w}\right)A \qquad (8)$$

where A is ^{222}Rn activity in water, H_c is the dimensionless Henry's law constant, and V_a/V_w is the average air-to-water volume ratio in the karst system. Integrating Eq. 8 over the transport time between the recharge area and the spring, the final ^{222}Rn activities for different discharge values are plotted in Figure 10b for $V_a/V_w = 0.1$ and 0.2. While this approach is simplistic, it demonstrates that the observed ^{222}Rn activity is influenced by degassing and that a relatively small volume of air in the system is sufficient to make a noticeable difference in ^{222}Rn activity.

4.7 Isotopic composition of sulfate

The stable isotopic signatures of dissolved SO$_4$ in spring water showed a seasonal trend, whereby the samples collected during spring freshet had lower values of δ^{34}S and δ^{18}O compared to the samples from late summer and winter (Figure 11a). These values are compared to the signatures of different sulphate sources delineated by Nightingale and Mayer (2011) based on a comprehensive literature review of studies investigating the isotopic composition of sulphate in precipitation, river and lake water, groundwater, soils, and rocks. The evaporite field was further constrained to the typical isotopic signatures of Devonian carbonates (δ^{34}S ranging 17–28 ‰; δ^{18}O ranging 10–17 ‰) (Claypool et al., 1980; Grasby, 1997). The seasonal pattern of isotope signature suggests a strong influence of SO$_4$ derived from the oxidation of sulfide minerals during the snowmelt period and a substantial contribution of evaporite during fall and winter (Figure 11a).
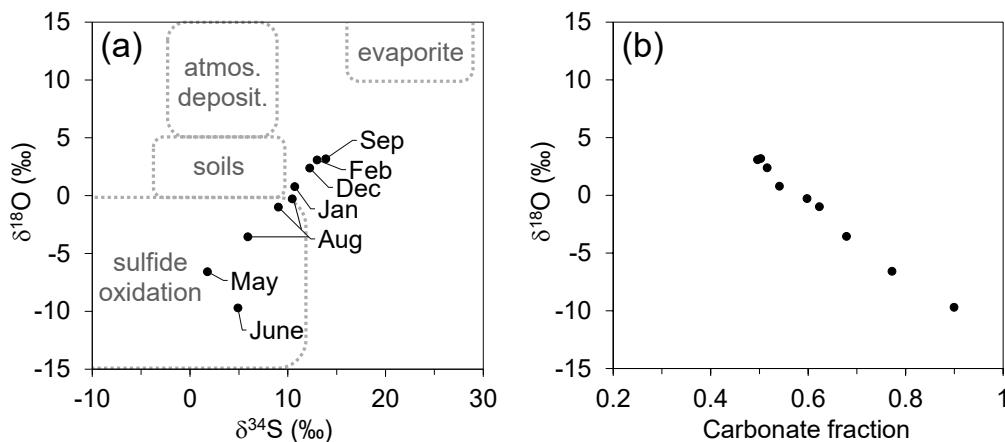
Figure 11 (a) Relation between stable isotope ratios of sulfur (δ^{34}S) and oxygen (δ^{18}O) in dissolved sulfate in spring samples during August 2021 and September 2022, with dashed lines indicating the composition fields of potential sulfate sources (Nightingale and Mayer, 2011). (b) Relation between carbonate fraction in water and δ^{18}O in sulfate.

The δ^{18}O values of dissolved SO_4 had a linear relation with the carbonate fraction of water (Figure 11b), suggesting the

415 mixing of two components of water. Since high carbonate fraction was observed during the high-flow period (Figure 8b), this component represents snowmelt recharge. The component with low carbonate fraction represents groundwater released from over-winter storage, which is presumably in contact with evaporite deposits within the Palliser Fm.

4.8 Annual water balance

420 To examine the water balance of the karst system, annual precipitation recorded at Burstall Pass AWS was compared against total annual discharge of the WKS for hydrological years 2017–2023. The discharge was expressed in mm by dividing it by the effective catchment area of 18 km² (see Section 4.2). Total annual discharge was strongly correlated with annual precipitation (Figure 12a). This is expected as the majority discharge occurred during May–August, when the flow was driven by snowmelt and summer rain (Figure 8a). After this high-flow period, the spring discharge was mostly sustained

425 by the release of groundwater stored within the system.

The amount of storage release can be assessed by examining the amount of post-freshet flow, defined as the total flow between the hydrochemical transition point (see Section 4.3) and the beginning of freshet in the following year. There was no obvious correlation between total precipitation and post-freshet discharge (Figure 12b), suggesting that the total amount of precipitation has relatively little influence on the amount of groundwater stored in the system after the hydrochemical

430 transition point. This can be explained if it is assumed that the hydrological input to the karst system is far greater than the storage capacity, resulting in the full capacity of groundwater at the hydrochemical transition point regardless of the input amount. Similar observations are made in alpine aquifers consisting of Quaternary sediments (Hayashi, 2020). The average of post-freshet flow over seven years was 410 mm (Figure 12b), which is similar to the intercept (= 420 mm) of the linear relation between total precipitation and total discharge (Figure 12a). It is not clear if this is merely a coincidence, or if it

435 indicates the influence of storage capacity on the annual water balance.
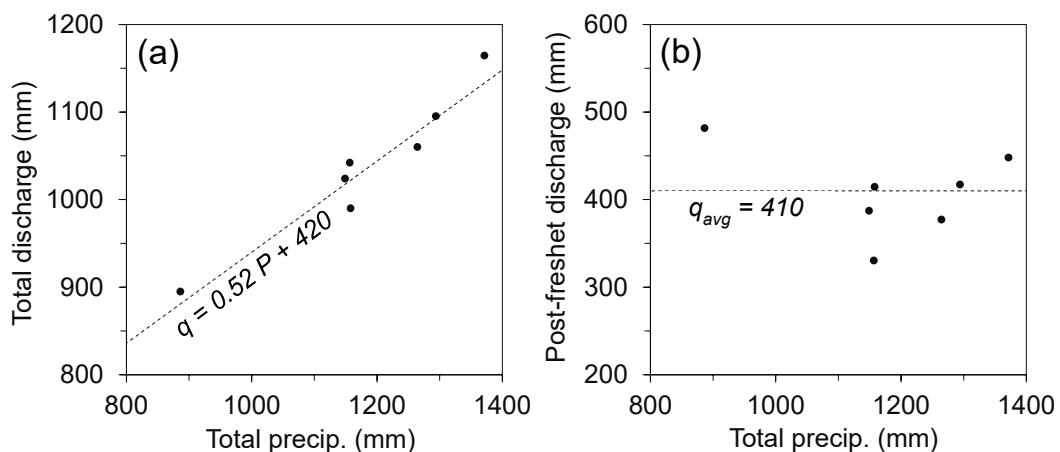
Figure 12 (a) Relation between total precipitation and discharge of hydrological years (1 November – 31 October) of 2017–2023, with the dashed line indicating a linear relation determined by the least-squares regression. (b) Relation between total precipitation and the post-freshet discharge after the hydrochemical transition point. The dashed line indicates the average of seven years.

5 Discussions

440

5.1 Groundwater flow velocity and the spring system response time

Three rate variables were identified regarding the dynamics of the spring system: solute transport velocity (Figure 5b), transport response time (Figure 7d), and hydraulic response time (Figure 7c). For solute transport, the velocity determined by dye tracer tests and the response time determined by the analysis of diel EC signals gave consistent results (Figure 7d)

445 indicating the inverse relation between velocity and response time. Transport velocity does not generally represent the water flow velocity in karst conduits because there are other processes that can delay the transport, even for chemically conservative tracers, and cause physical retardation of solutes as discussed below. Hydraulic response time reflects the rate of energy propagation, rather than water itself, and is not directly related to flow velocity. In some literature, the energy propagation rate is referred to as celerity (Worthington and Foley, 2021).

450 Groundwater flow in karst conduits generally has a high Reynolds number ($> 10^2 - 10^3$) and hence, does not obey the Darcy's law (Worthington and Soley, 2017). Conduit flow is commonly conceptualized as open-channel flow using the Manning equation or turbulent flow in a saturated pipe using the Darcy-Weisbach equation. Inferring from a relatively low air-to-water volume ratio suggested by ^{222}Rn data (Figure 10b), it is assumed that most of the conduit flow occurs under pipe-flow conditions.

455 Following the approach of Jeannin (2001), discharge Q_p (m^3 s^{-1}) and velocity v_p (m s^{-1}) of turbulent flow through a pipe is estimated by the Darcy-Weisbach equation:

$$Q_p = -k' A_p \sqrt{\frac{dh}{dl}} \qquad \text{and} \qquad v_p = Q_p / A_p \qquad\qquad (9)$$

where A_p (m^2) is the pipe cross-sectional area, dh/dl is the hydraulic gradient, and k' (m s^{-1}) is the effective hydraulic conductivity for turbulent flow estimated by:

460 $\qquad k' = K_s R_h^{2/3}$ $\qquad\qquad\qquad\qquad\qquad\qquad\qquad\qquad (10)$

where K_s (m$^{1/3}$ s^{-1}) is a roughness coefficient and R_h (m) is the hydraulic radius equal to A_p divided by wetted perimeter of the pipe. For a circular pipe, R_h is equal to 1/4 of the pipe diameter. It is difficult to estimate the hydraulic gradient of the conduit system, however, it can be inferred from previous studies of karst systems in rugged, mountainous terrains similar to the current study. For example, in the Canadian Rockies, a map of the Castleguard Cave (Ford et al.,1983, Figure 3) suggests a

465 gradient of ~0.03, and Smart (1988) indicated a gradient ~0.025 in the Maligne Karst system. Jennin (2001) indicated gradients ranging 0.0004 – 0.006 in the flat part of the conduit near the spring outlet in Hölloch cave in Switzerland. Based on these studies, a rough estimate of the gradient in the WKS system is 0.003 – 0.03. A mean value of the square root of gradient within the estimated range, $(dh/dl)^{1/2} \sim 0.11$, is used in the following calculation.

Assuming a K_s of 20 m$^{1/3}$ s^{-1} (Jeannin, 2001), Eqs. 9 and 10 give $Q_p = 0.3$ m^3 s^{-1} and $v_p = 0.7$ m s^{-1} for a pipe diameter of

470 0.72 m, and $Q_p = 2.8$ m^3 s^{-1} and $v_p = 1.2$ m s^{-1} for a pipe diameter of 1.7 m. These diameters are smaller than ~3.7 m measured by a cave diver at the spring outlet (Tom Crisp, unpublished data) but are reasonable, considering the enlargement of conduits connected to the outlet (Maqueda et al., 2023). While this calculation has a large degree of uncertainty, the flow velocity through the karst conduit network is expected to be on the order of 1 m s^{-1} during May–December when Q varies between 0.3 and 3 m^3 s^{-1}. A similar calculation for open-channel flow using the Manning equation gives the same order of

475 velocity (~1 m s^{-1}) for water depths ranging 0.1–1 m. At this magnitude of velocity, water would travel from BP14 to WKS in ~4 h. This is much shorter than observed transport response time (Figure 7d), indicating the presence of retardation mechanisms, most likely explained by large pools within the conduit network that stagnate the flow and cause mixing of water (Hauns et al., 2001). As an example, the transport response time of a well-mixed pool (T_{TR}, s) is related to Q and pool volume (V_{PL}, m^3) by:

480 $\qquad T_{TR} = V_{PL} / Q$ $\qquad\qquad\qquad\qquad\qquad\qquad\qquad\qquad (11)$

indicating that for a fixed number and volume of pools, T_{TR} increases as Q decreases. This can explain the observed increase in transport response time concurrent with the reduction in discharge (Figure 7d).

The propagation of hydraulic response in a saturated pipe is faster than flow velocity by orders of magnitude (Worthington, 2019), meaning that the diel fluctuations of discharge would have a delay of less than an hour between BP14 and WKS. This is contrary to the observed delay of 12–15 h (Figure 7c), suggesting that the pressure propagation in saturated conduits is interrupted by unsaturated sections (i.e. open channel), where the rate of hydraulic propagation is on the same order as the flow velocity (Bedient and Huber, 2002, p.272). In addition, the conduit network may be interrupted by the pools mentioned above, which can add further delay of hydraulic propagation. Therefore, it is possible that the hydraulic response time is mainly controlled by the configuration of the conduit network, which remains relatively static, not by the hydraulic gradient or flow velocity, resulting in only a slight increase in hydraulic response time over the season. Alternatively, the observed delay of hydraulic propagation is associated with the vertical flow of water from the ground surface to the conduit system. Similar magnitude of delay of diel discharge fluctuations was reported by Smart and Ford (1986) at a glacier-fed karst spring of Castleguard Cave, located ~190 km northwest of the WKS.

5.2 Transition of hydrochemical characteristics in late summer

Two distinct phases were observed in the chemical composition of spring water. The first phase occurred during the high-flow period in May–August, when discharge was sustained above ~1000 L s^{-1} by snowmelt recharge, and was characterized by high Ca/Mg and carbonate fraction (Figure 8b) and the sulfate isotopic composition influenced by sulfide oxidation (Figure 11). This likely represents the interaction of snowmelt with calcite-saturated water in the rock matrix of Exshaw and Palliser Fms. (Figure 1). The isotopic composition shifted only slightly towards the signature of snowmelt (Figure 8c) from the over-winter composition, indicating the dominance of water stored in the matrix for at least a year, most likely longer. This is consistent with the tritium content suggesting a residence time of multiple years (Figures 8d and 9).

The second phase starts after the hydrochemical transition point when the flow regime shifts from high flow with strong diel fluctuations to low flow with weak diel fluctuations (~20 July in Figures 7a and 7b). The Ca/Mg is constant (= 2) during the second phase, and carbonate fraction is stable. The sulfate isotopic composition of this water is more strongly influenced by anhydrite dissolution compared to the first phase (Figure 11). It represents the over-winter drainage of water stored in the deeper part of Palliser Fm. The amount of over-winter drainage is consistent from year to year at ~410 mm (Figure 12b). Based on the relatively small shift of stable isotopic composition in the first phase, the total over-winter storage is expected to be much greater than 410 mm.

The transition of chemical composition is concurrent with a distinct change in the diel fluctuations of discharge and EC as demonstrated in Figure 6d, whereby the fluctuation magnitude of discharge decreases and that of EC increases. The timing of transition coincided with the complete disappearance of snowcover from the Burstall Pass plateau near BP11, where a series of satellite images (Planet Team, 2025) indicated that snowcover disappeared between 15 and 25 July (Figure 13). Similarly, the snowcover disappeared from the plateau between 5 and 12 August in 2020 (Figure A3), coinciding with the hydrochemical transition (Figure A1). Therefore, the hydrochemical transition represents the shift of the dominant source of diel signals from widespread snowmelt recharge in the plateau area to point recharge of glacier melt water. The former has a strong influence on discharge fluctuations because the amount is much greater than glacier input, but a weak influence on EC because dilute snowmelt water is mixed with the carbonate-rich matrix water before it enters the conduit system. In contrast, the latter sends glacier melt water directly to the conduit and has a stronger influence on EC fluctuations.
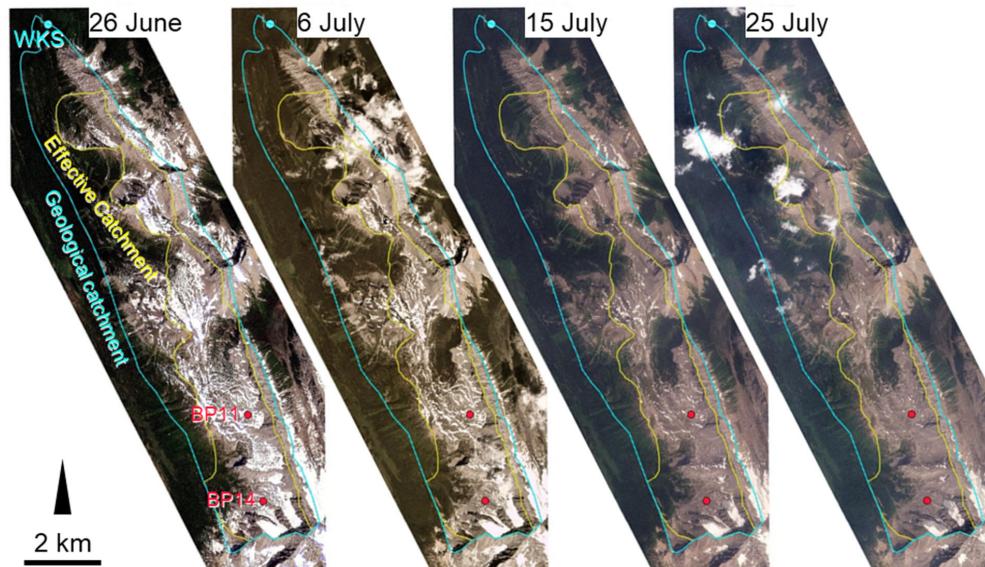
Figure 13 Satellite images of the potential recharge areas of the Watridge Karst Spring (WKS) on 26 June, 6 July, 15 July, and 25 July of 2021. The images show the tracer release locations (BP11 and BP14), the geological catchment, and the effective catchment (Figure 1a). Image source: Planet Team (2025).

5.3 Conceptual hydrogeological model

The study started with no information on the karst system aside from the location of the WKS. A broad range of data collected over seven hydrological years can now be used to develop a conceptual hydrogeological model (Figure 14). A reasonably fast arrival of dye tracer plumes clearly shows that the WKS is connected to a network of conduits, yet the transport velocity (0.05 – 0.15 m s⁻¹) is much slower than the order of velocity (1 m s⁻¹) expected for conduit flow or open-channel flow. Therefore, there likely are many pools within the conduit network, causing the physical retardation of solute transport. Two distinct phases of water chemistry indicate mixing of the over-winter component stored in the matrix within the deeper part of the system (Figure 14b) with snowmelt infiltration from the near-surface zone. Snowmelt infiltration is mixed with carbonate-rich water in the epikarst zone (Figure 14a), resulting in muted diel EC fluctuations. In contrast, the hydraulic signals are conveyed vertically down in the saturated matrix and conduits, resulting in pronounced diel discharge signals similar to those observed in non-karst alpine aquifers (e.g., Muir et al., 2011).

The flow in the conduit network increases downstream from the uppermost part of the catchment (near BP14) to the spring outlet as more water is added through combination of diffuse and point recharge. The conduit network likely includes saturated parts acting like pipes, unsaturated parts acting like open channels, and many pools delaying solute transport and hydraulic responses. The karst system likely has multiple levels of conduits (Figure 14) with bifurcation points as indicated by multiple arrivals of tracer plume (Figure 5a). The multi-level karst system inferred in this study is consistent with previous alpine karst studies including the karst networks of Crowsnest Pass (Worthington, 1991) and Maligne Canyon (Smart, 1988) in the Canadian Rockies, the Lurbach-Tanneben karst aquifer in Austria (Birk et al., 2014; Kübeck et al., 2013), and the Bullock Creek karst aquifer in New Zealand (Crawford, 1989).
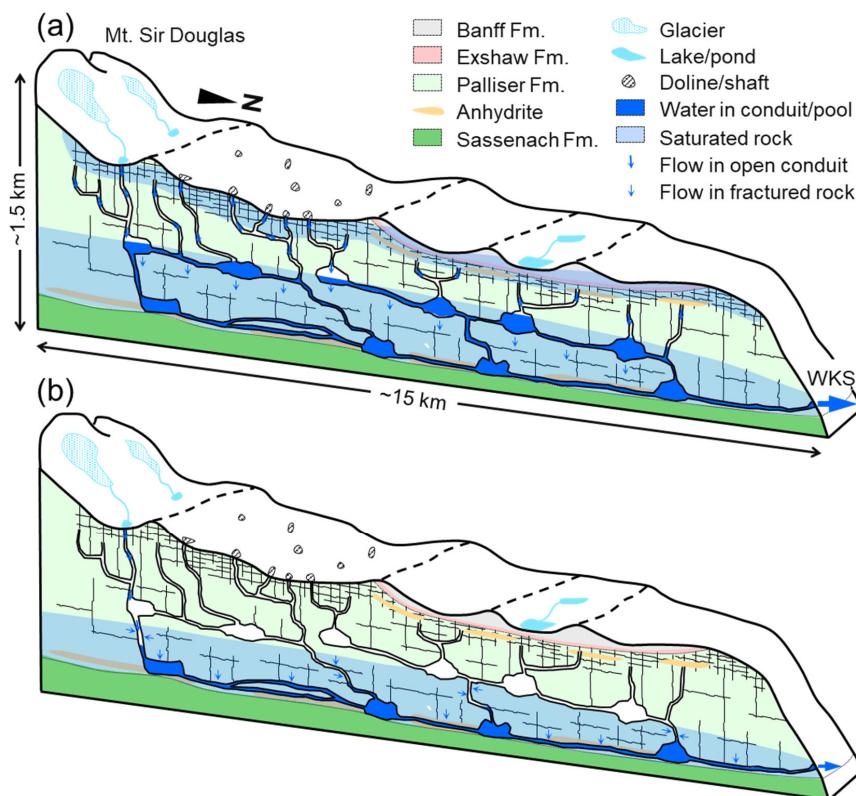
Figure 14 The conceptual cross section of the karst system feeding the Watridge Karst Spring (WKS), showing geological units and possible configuration of conduit network consisting of saturated pipes, open channels, and pools retarding solute transport. (a) Inferred condition during the spring freshet depicting the snowmelt infiltration saturating the epikarst zone. Upper part of conduit system is transmitting snowmelt water rapidly to the saturated conduits. (b) Inferred condition after the hydrochemical transition point depicting the absence of distributed snowmelt infiltration. The remaining groundwater in the deeper zone is gradually drained until the next freshet.

6 Conclusions

545

Rugged and inaccessible terrains are major challenges in alpine karst hydrogeology. This study is an attempt to characterize the hydrogeological behaviour of an alpine karst system, starting from no local information other than the location of the spring outlet. Using geological maps and simple water balance, aided by dye tracer tests at two locations, it was possible to estimate the extent of the catchment of the spring. The dominance of snowmelt in water input provided a

550 unique opportunity to use the diel signal of discharge and electrical conductivity (EC) resulting from distinct diel cycles of snowmelt. The diel signal analysis showed that the solute transport time from recharge areas to the spring (i.e. transport response time) gradually increased over the summer and fall, while the hydraulic response time of discharge remained relatively constant. This implies that the transport response time is controlled by the magnitude of discharge, while the hydraulic response time is controlled by the configuration of conduit network. High-frequency sampling and analysis of

555 chemical and isotopic composition of spring water demonstrated that the karst system is characterized by mixing of over-winter water and seasonal snowmelt water. The isotopic composition of spring water is relatively insensitive to snowmelt input having lighter isotopic composition, indicating that a large volume of water is stored in the fractured rock matrix between the ground surface and the karst conduits. Total discharge volume during the low-flow period after freshet was

uncorrelated with annual precipitation, suggesting that the storage volume in rock matrix is large enough to buffer the effects
560 of interannual precipitation variability, and potentially the effects of climate warming affecting the seasonal pattern of
precipitation.

The methods developed in this study are expected to be applicable to alpine karst systems in other parts of the world
having a distinct snowmelt season generating the diel signals. Combined with geological information, satellite images, and a
limited number of tracer tests, the suite of tools presented here can provide an effective approach for characterizing karst
565 hydrogeology in remote, inaccessible terrains. The quantitative analysis in this study was limited to simple differential
equations. In the future, more advanced numerical flow and transport models may be used to develop further insights into the
possible configuration of the karst system and its response to snowmelt inputs.

570

Appendix A: Supplementary figures
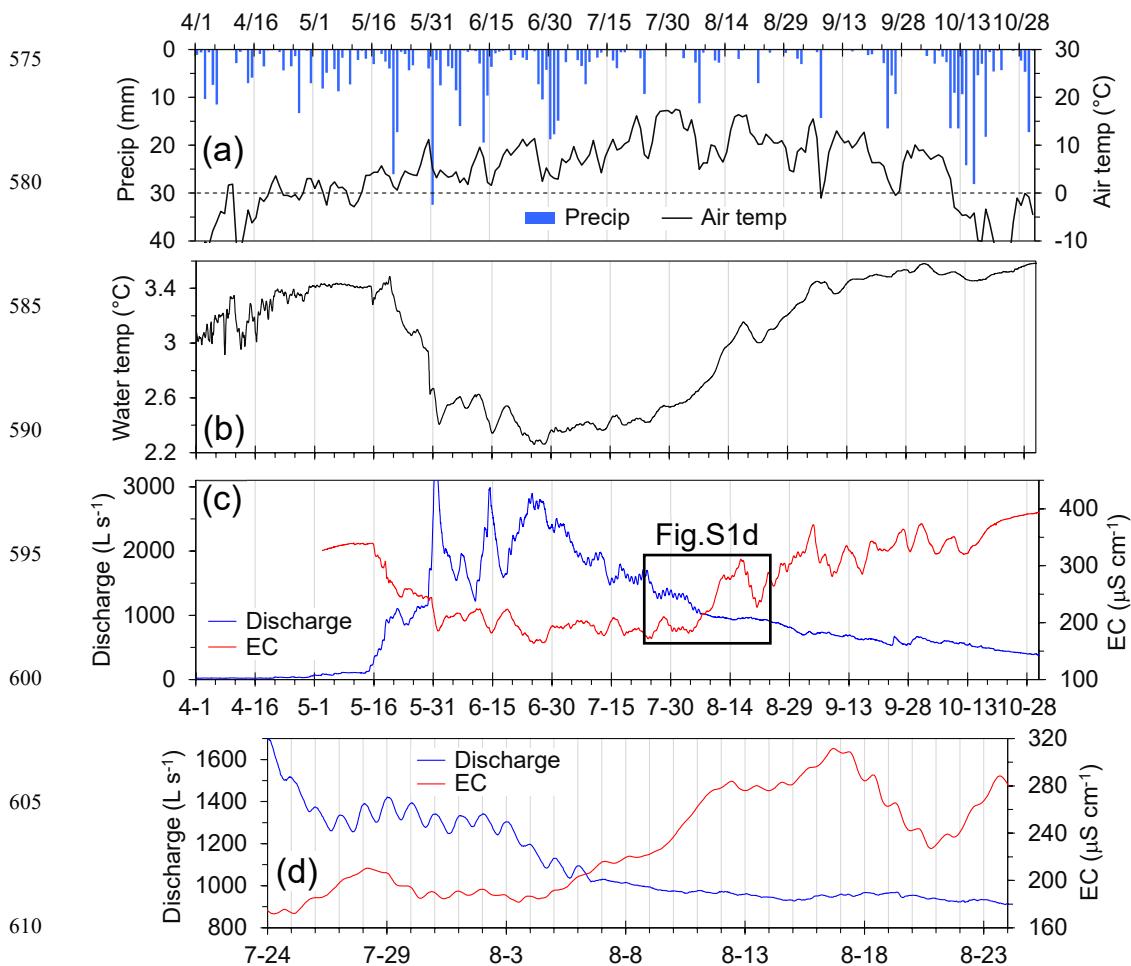
Figure A1 (a) Daily total precipitation and daily mean air temperature measured at the Burstall Pass weather station, 1 April
– 31 October 2020. (b) Water temperature at the spring outlet. (c) Spring discharge and electrical conductivity (EC). (d)
615 Spring discharge and EC during 24 July – 24 August 2020.
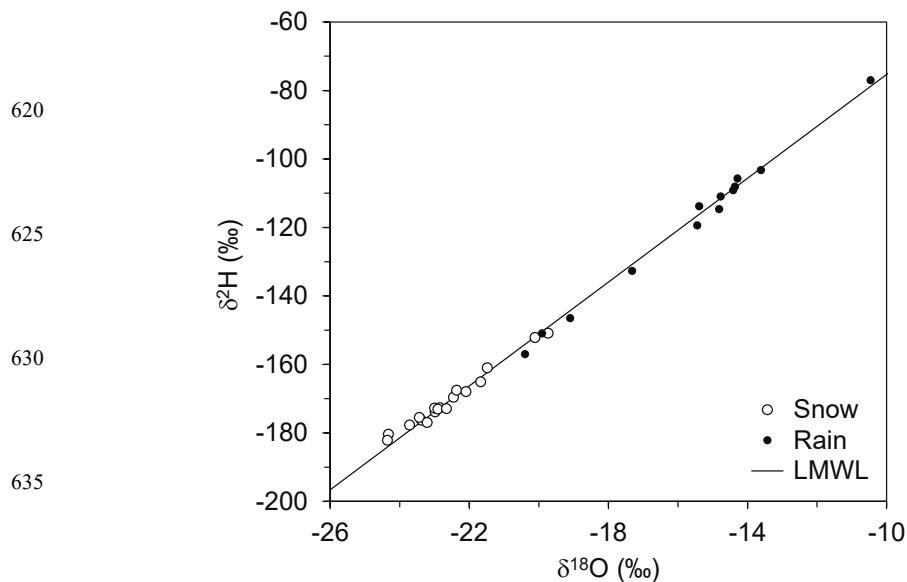
Figure A2 Isotopic composition of rain samples collected at the spring and snow samples collected at the spring or its vicinity (< 4 km). The local meteoric water line (LMWL) was derived from all precipitation samples that were collected during this study.
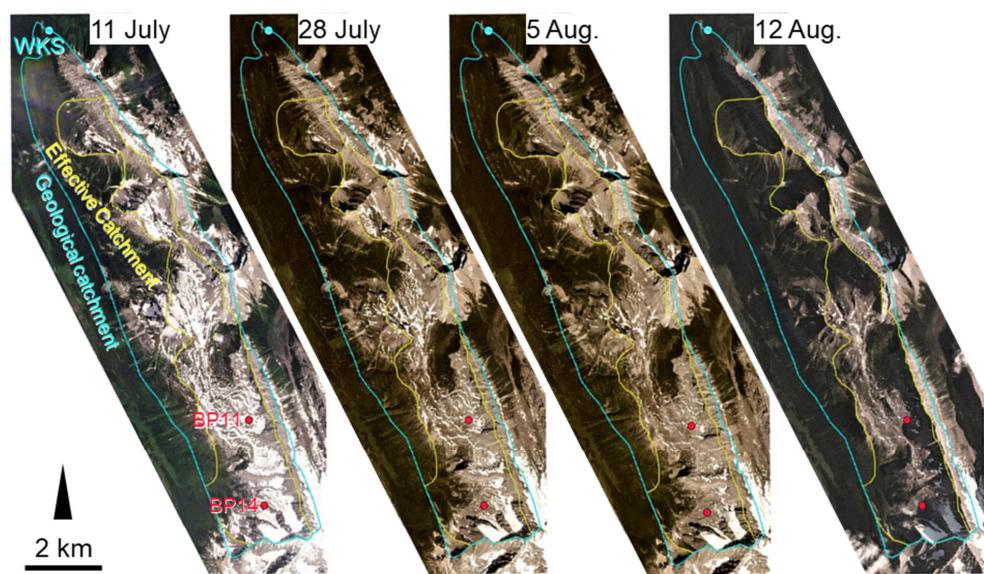
Figure A3 Satellite images of the potential recharge areas of the Watridge Karst Spring (WKS) on 11 July, 28 July, 5 August, and 12 August of 2020. The images show the tracer release locations (BP11 and BP14 the geological catchment, and the effective catchment (Figure 1a). Image source: Planet Team (2025).
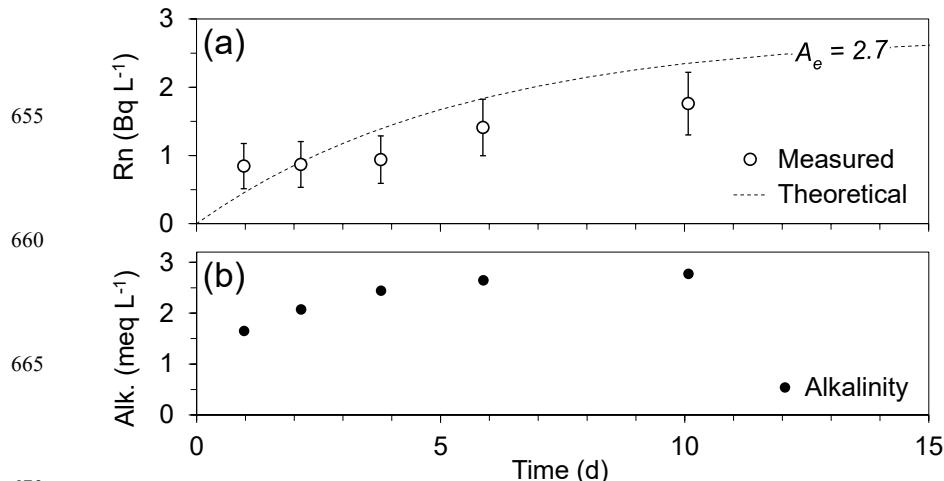
Figure A4 (a) Previously unpublished data of ^{222}Rn activity during a laboratory experiment conducted in 2016 using Palliser limestone fragments collected from a talus slope in the Hathataga Creek watershed (Christensen et al., 2020). Error bars indicate the analytical uncertainty. Pebble-sized (diameter 5-30 mm), angular rock fragments were mixed with deionized water in a sealed 2.5-L glass jar and kept in a laboratory at a temperature of ~22 °C. The porosity of water-rock mixture was 0.45. For each measurement, a 320-mL water sample was collected from the jar and poured back in the jar after the measurement. Prior to the measurements shown in the graph, the same water-rock mixture was left in the laboratory for 147 days to determine the steady-state activity (A_e) of the system. This value is used in Eq. 7 to calculate the theoretical values shown in the graph. Except for the first sample, measured values were lower than theoretical values, most likely due to the loss of dissolved ^{222}Rn during measurements. (b) Alkalinity of water samples during the same experiment demonstrating the gradual dissolution of calcite in the initially ion-free water. The equilibrium alkalinity was 6.8 meq L^{-1}.

Appendix B: Equation representing ^{222}Rn decay in a closed water-rock system

When a closed system consisting of the rocks containing a source of ^{222}Rn is saturated with ^{222}Rn-free water, the evolution of ^{222}Rn activity (A, Be L^{-1}) can be described by a simple mass balance equation:

$$nV\frac{dA}{dt} = Sf - nV\lambda A \qquad (B1)$$

where n is porosity, V (m^3) is the total volume of the system, S (m^2) is the total area of rock surfaces emitting ^{222}Rn, f (Bq s^{-1} m^{-2}) is the flux density of freshly produced ^{222}Rn expressed as the equivalent activity, and λ (s^{-1}) is the decay coefficient. Equation A1 can be rearranged to:

$$\frac{dA}{dt} = \frac{S_V f}{n} - \lambda A \qquad (B2)$$

where S_V (m^{-1}) is the volume-specific surface area (= S/V). The solution to Eq. A2 with the initial condition, $A = 0$ at $t = 0$, is:

$$A(t) = (S_V f / n) [1 - \exp(-\lambda t)] \qquad (B3)$$

which reduces to

$$A(t) = A_e [1 - \exp(-\lambda t)] \qquad (7)$$

by equating the leading term with A_e (Bq L$_{-1}$), which is the ^{222}Rn activity at steady state (Hoehn et al., 1992, Eq.1).

Therefore, for water-rock systems consisting of a particular type of rock (e.g., Palliser limestone) having a similar ^{222}Rn flux density, A_e generally increases as specific area increases and porosity decreases.

Data availability. The data that support the findings of this study are available from the corresponding author upon reasonable request.

705 **Author contribution.** Both authors participated in the conceptualization, methodology, experimental design, data acquisition and analysis, and manuscript preparation.

Competing interests. The authors declare that they have no conflict of interest.

710 **Acknowledgement.** We thank David Geuder, Brandon Hill, and Evan Sieben for pre-2020 field data collection; Quinn Decent, Sophie Prevost, and numerous others for field assistance; Steve Worthington and Margot McMechan for helpful discussion; Charles Yonge for inspiration; Tom Crisp for making unpublished data available; and Parks Canada and Alberta Parks for research permits. This article is dedicated to the memory of Larry Bentley, who initiated the study with MH in 2016 and provided constructive suggestions throughout. Funding for the study was provided by Canada First Research
715 Excellence Fund (Global Water Futures), Alberta Innovates (Water Innovation Program), and Natural Sciences and Engineering Research Council.

References

720 Alberta Climate Information Service (ACIS): Current and Historical Alberta Weather Station Data Viewer. https://acis.alberta.ca/acis/weather-data-viewer.jsp (last access: 30 May 2025), 2025.

Andrichuk, J. M.: Facies analysis of Upper Devonian Wabamun Group in west-central Alberta, Canada. Bulletin of the American Association of Petroleum Geologists, 44, 1651–1681, 1960.

Beales, F.: Conditions of deposition of Palliser (Devonian) Limestone of southwestern Alberta. Bulletin of the American Association of Petroleum Geologists, 40, 848–870, 1956.

725 Bedient, P. B. and Huber, W. C.: Hydrology and Floodplain Analysis, 3rd ed. Prentice-Hall, Upper Saddle River, New Jersey. 763 pp., 2002.

Birk, S., Wagner, T., and Mayaud, C. Threshold behavior of karst aquifers; the example of the Lurbach karst system (Austria). Environmental Earth Sciences, 72, 1349–1356, doi:10.1007/s12665-014-3122-z, 2014.

Canadian Rockies Hydrological Observatory (CRHO). Air temperature and precipitation data from Burstall Pass
730 hydrometeorological station, Canadian Rockies Hydrological Observatory, University of Saskatchewan. https://giws1.usask.ca/applications/public.html (last access: 30 May 2025), 2025.

Chen, Z., Auler, A. S., Bakalowicz, M., Drew, D., Griger, F., Hartmann, J., Jiang, G., Moosdorf, N., Richts, A., Stevanovic, Z., Veni, G., and Goldscheider, N.: The World Karst Aquifer Mapping project: concept, mapping procedure map of Europe. Hydrogeology Journal, 25, 771–785. doi:10.1007/s10040-016-1519-3, 2017.

735 Christensen, C. W., Hayashi, M., and Bentley, L. R.: Hydrogeological characterization of an alpine aquifer system in the Canadian Rocky Mountains. Hydrogeology Journal, 28: 1871–1890, 2020.

Clark, L. M.: Geology of Rocky Mountain Front Ranges near Bow River, Alberta. Bulletin of the American Association of Petroleum Geologists, 33, 614–633, 1949.

Claypool, G. E., Holser, W. T., Kaplan, I. R., Sakai, H., and Zak, I.: The age curves of sulfur oxygen isotopes in marine
740 sulfate and their mutual interpretation. Chemical Geology, 28, 199–260. doi:10.1016/0009-2541(80)90047-9, 1980.

Crawford, S.: Karst research in the Paparoa National Park - the hydrological behaviour of a high flooding frequency karst system in New Zealand. Proceedings of the 8th ACKMA Conference, Punakaiki, New Zealand, 1989. http://st1.asflib.net/MEDIA/ASF-CD/ASF-M-00185/ackcd/proceed/08/content.html, 1989.

de Wit, R. and McLaren, D. J.: Devonian sections in the Rocky Mountains between Crowsnest Pass and Jasper, Alberta.
745 Paper, 50-23. Geological Survey of Canada, 1950.

Dingman, S. L.: Physical Hydrology, 2nd ed., Wavel Press, Long Grove, IL., 2002.

Domenico, P. A. and Schwartz, F. W.: Physical and Chemical Hydrogeology, 2nd ed., John Wiley Sons Inc., New York, 1998.

Downing, D. J. and Pettapiece, W. W.: Natural regions and subregions of Alberta. Natural Regions Committee. Government
750 of Alberta. Pub. No. T/852, 2006.

Drake, J. and Ford, D.: Solutional erosion in the southern Canadian Rockies. Canadian Geographer, 20, 158–170, doi:10.1111/j.1541-0064.1976.tb00228.x, 1976.

Durridge Company Inc.: CAPTURE. RAD7 data acquisition and analysis. https://d3pcsg2wjq9izr.cloudfront.net/files/31376/download/462053/CaptureManual.pdf, 2014.

755 Eisenlohr, L. and Surbeck, H.: Radon as a natural tracer to study transport processes in a karst system: An example in the Swiss Jura. Comptes rendus de l'Académie des Sciences, Paris, t.321, Série IIa, 761–767, 1995.

Environment and Climate Change Canada (ECCC): Canadian Historical Weather Radar. https://climate.weather.gc.ca/radar/index_e.html (last access: 27 January 2025), 2025.

Field, M. S. and Nash, S. G.: Risk assessment methodology for karst aquifers: (1) Estimating karst conduit-flow parameters.
760 Environmental Monitoring and Assessment, 47, 1–21, 1997.

Fiorillo, F., and Doglioni, A.: The relation between karst spring discharge and rainfall by cross-correlation analysis (Campania, Southern Italy). Hydrogeology Journal, 18, 1881–1895. doi:10.1007/s10040-010-0666-1, 2010.

Ford, D. C.: Alpine karst in the Mt. Castleguard-Columbia Icefield area, Canadian Rocky Mountains. Arctic and Alpine Research, 3, 239–252, 1971a.

765 Ford, D. C.: Characteristics of limestone solution in the Southern Rocky Mountains and Selkirk Mountains, Alberta British Columbia. Canadian Journal of Earth Sciences, 8, 585–609, 1971b.

Ford, D. C.: Effects of glaciations upon karst aquifers in Canada. Journal of Hydrology, 61, 149–158, 1983a.

Ford, D. C.: The physiography of the Castleguard Karst and Columbia Icefields area, Alberta, Canada. Arctic and Alpine Research, 15, 427–436, 1983b.

770 Ford, D. C., Smart, P. L., and Ewers, R. O.: The physiography and speleogenesis of Castleguard Cave, Columbia Icefields, Alberta, Canada. Arctic and Alpine Research, 15, 437–450, 1983.

Ford, D. and Williams, P. Karst Hydrogeology and Geomorphology. John Wiley and Sons, 562 pp, 2007.

Fox, F. G.: Devonian stratigraphy of Rocky Mountains and foothills between Crowsnest Pass Athabasca River, Alberta, Canada. Bulletin of the American Association of Petroleum Geologists, 35, 822–843, 1951.

775 Goldscheider, N., Meiman, J., Pronk, M., and Smart, C.: Tracer test in karst hydrogeology and speleology. International Journal of Speleology, 37, 27–40. doi:10.5038/1827-806X.37.1.3, 2008.

Goldscheider, N.: A holistic approach to groundwater protection and ecosystem services in karst terrains. Carbonates and Evaporites, 9, 1241–1249. doi:10.1007/s13146-019-00492-5, 2019.

Goldscheider, N., Chen, Z., Auler, A. S., Bakalowicz, M., Broda, S., Drew, D., Harman, J., Jiang, G., Stevanovic, Z., and
780 Veni, G.: Global distribution of carbonate rocks and karst water resources. Hydrogeology Journal, 28, 1661–1677. doi:10.1007/s10040-020-02139-5, 2020.

Govett, G. J. S.: Occurrence and stratigraphy of some gypsum and anhydrite deposits in Alberta. Research Council of Alberta, Bulletin 7, 1961.

Grasby, E. S.: Controls on the Chemistry of the Bow River, Southern Alberta, Canada, Ph.D. Thesis, University of Calgary, doi:10.11575/PRISM/15509, 1997.

Gremaud, V., Goldscheider, N., Savoy, L., Favre, G., and Masson, H.: Geological structure, recharge processes and underground drainage of a glacierised karst aquifer system, Tsanfleuron-Sanetsch, Swiss Alps. Hydrogeology Journal, 17, 1833–1848, doi:10.1007/s10040-009-0485-4, 2009.

Hauns, M., Jeannin, P.-Y., and Atteia, O.: Dispersion, retardation and scale effect in tracer breakthrough curves in karst conduits. Journal of Hydrology, 241, 177–193, 2001.

Hayashi, M.: Temperature-electrical conductivity relation of water for environmental monitoring and geophysical data inversion. Environmental Monitoring and Assessment, 96, 121–130, 2004.

Hayashi, M.: Alpine hydrogeology: The critical role of groundwater in sourcing the headwaters of the world. Groundwater, 58, 498–510, 2020.

He, J. and Hayashi, M.: Field observation and mathematical representation of the hydrogeological function of alpine landforms in the Canadian Rockies. Hydrological Processes, 37, e14881, 2023.

Hoehn E., von Gunten, H. R., Stauffer, F., and Dracos, T.: Radon-222 as a groundwater tracer: A laboratory study. Environmental Science and Technology, 26, 734–738, 1992.

Holter, M. E.: Limestone Resources of Alberta. Economic Geology Report 4. Alberta Research Council, 1976.

Hood, J. L. and Hayashi, M.: Characterization of snowmelt flux and groundwater storage in an alpine headwater basin. Journal of Hydrology, 521, 482–497, 2015.

Hood, J. L., Roy, J. W., and Hayashi, M.: Importance of groundwater in the water balance of an alpine headwater lake. Geophysical Research Letters, 33, L13405, doi:10.1029/2006GL026611, 2006.

Howell, B. A., Fryar, A. E., Benaabidate, L., Bouchaou, L., and Farhaoui, M.: Variable responses of karst springs to recharge in the Middle Atlas region of Morocco. Hydrogeology Journal, 27, 1693–1710. doi:10.1007/s10040-019-01945-w, 2019.

International Atomic Energy Agency (IAEA): Water Isotope System for Electronic Retrieval. https://nucleus.iaea.org/wiser/ (last access: 30 May 2025), 2025.

Jeannin, P.-Y.: Modeling flow in phreatic and epiphreatic karst conduits in the Hölloch Cave (Muotatal, Switzerl). Water Resources Research, 37, 191–200, doi:10.1029/2000WR900257, 2001.

Jódar, J., González-Ramón, A., Martos-Rosillo, S., Heredia, J., Herrera, C., Urrutia, J., Caballero, Y., Zabaleta, A., Antigüedad, I., Custodio, E., and Lambán, L. J.: Snowmelt as a determinant factor in the hydrogeological behaviour of high mountain karst aquifers: The Garcés karst system, Central Pyrenees (Spain). Science of the Total Environment, 748. doi:10.1016/j.scitotenv.2020.141363, 2020.

Kovačič, G.: Hydrogeological study of the Malenščica karst spring (SW Alovenia) by means of a time series analysis. Acta Carsologica, 39, 201–215. doi:10.3986/ac.v39i2.93, 2010.

Krainer, K., Winkler, G., Pernreiter, S., and Wagner, T. Unusual catchment runoff in a high alpine karst environment influenced by a complex geological setting (Northern Calcareous Alps, Tyrol, Austria). Hydrogeology Journal, 29, 2837–2852. doi:10.1007/s10040-021-02405-0, 2021.

Kübeck, C., Maloszewski, P. J., and Benischke, R.: Determination of the conduit structure in a karst aquifer based on tracer data-Lurbach system, Austria. Hydrological Processes, 27, 225–235. doi:10.1002/hyp.9221, 2013.

Lachmar, T., Sorsby, S., and Newell, D.: Geochemical insights into groundwater movement in alpine karst, Bear River Range, Utah, USA. Hydrogeology Journal, 29, 687–701, doi:10.1007/s10040-020-02256-1, 2021.

Lilley, S.: Karst Hydrogeology in the Spray Mountains of Kananaskis, Alberta, Canada. MSc. Thesis, University of Calgary, 140 pp., doi.org/10.11575/PRISM/41999, 2023.

Lilley, S and Crisp, T.: The Watridge Spring: Divers and scientists join to unveil an underestimated cave network. The Canadian Caver, 91, 5–10, 2022.

MacDonald, M. K., Pomeroy, J. W., and Pietroniro, A.: On the importance of sublimation to an alpine snow mass balance in the Canadian Rocky Mountains. Hydrology and Earth System Sciences, 14, 1401–1415, 2010.

MacNeil, D. J.: Stratigraphy and Structure of Moose Mountain Area, Alberta. Bulletin of the American Association of Petroleum Geologists, 27, 38–50, 1943.

Mangin, A.: Use of autocorrelation and spectral analyses to obtain a better understanding of hydrologic systems. Journal of Hydrology, 67, 25–43, 1984.

Maqueda, A., Renard, P., and Filipponi, M.: Karst conduit size evolution using speleogenesis modelling. Environmental Earth Sciences, 82, 360. doi:10.1007/s12665-023-11035-6, 2023.

McMechan, M. E.: Geology, Spray Lakes Reservoir, Alberta – British Columbia, Geological Survey of Canada, Canadian Geoscience Map 14, scale 1:50 000. doi:10.4095/288954, 2012.

Muir, D. L., Hayashi, M., and McClymont, A. F.: Hydrological storage and transmission characteristics of an alpine talus. Hydrological Processes, 25, 2954–2966, 2011.

Mull, D. S., Liebermann, T. D., Smoot, J. L., and Woosley, L. H.: Application of dye-tracing techniques for determining solute-transport characteristics of groundwater in karst terranes. Rep. EPA 904/6-88-001, U.S. Environmental Protection Agency, Atlanta, Georgia.,103 pp., 1988.

Nightingale, M., and Mayer, B.: Identifying sources and processes controlling the sulphur cycle in the Canyon Creek watershed, Alberta, Canada. Isotopes in Environmental and Health Studies, 48, 89–104. doi:10.1080/10256016.2011.631704, 2012.

Peano, G., Vigna, B., Villavecchia, E., and Agnesod, G.: Radon exchange dynamics in a karst system investigated by radon continuous measurements in water: First results. Radiation Protection Dosimetry, 145, 173–177, doi:10.1093/rpd/ncr053, 2011.

Planet Team: Planet Application Program Interface: In Space for Life on Earth. San Francisco. https://api.planet.com, 2025.

850 Rahnemaei, M., Zare, M., Nematollahi, A. R., and Sedghi, H.: Application of spectral analysis of daily water level and spring discharge hydrographs data for comparing physical characteristics of karstic aquifers. Journal of Hydrology, 311, 106–116, doi:10.1016/j.jhydrol.2005.01.011, 2005.

Rosenberry, D. O. and Hayashi, M.: Assessing and Measuring Wetland Hydrology. In J. T. Anderson and C. A. Davis (Eds.), Wetland Techniques: Volume 1: Foundations (p. 87–225), doi:10.1007/978-94-007-6860-4_3, 2013.

855 Savanna River National Laboratory (SRNL): Recommended Henry's Law constant for non-groundwater pathways models in GoldSim. https://www.nrc.gov/docs/ML2020/ML20206L161.pdf, 2017.

Schäffer, R., Sass, I., and Heldmann, C. D.: Water supply in times of climate change –Tracer tests to identify the catchment area of an Alpine karst spring, Tyrol, Austria. Arctic, Antarctic, and Alpine Research, 52, 70–86. doi:10.1080/15230430.2020.1723853, 2020.

860 Smart, C. C.: The hydrology of the Castleguard karst. Arctic and Alpine Research, 15, 471–486, 1983.

Smart, C. C., and Ford, D. C.: Structure and function of a conduit aquifer. Canadian Journal of Earth Sciences, 23, 919–929, 1986.

Smart, C. C.: Quantitative tracing of the Maligne karst system, Alberta, Canada. Journal of Hydrology, 98, 185–204, 1988.

Smith, C. D., Mekis, E., Hartwell, M., and Ross, A.: The hourly wind-bias-adjusted precipitation data set from the
865 Environment and Climate Change Canada automated surface observation network (2001-2019). Earth System Science Data, 14, 5253–5265, doi:10.5194/essd-14-5253-2022, 2022.

Stevanović, Z.: Karst waters in potable water supply: a global scale overview. Environmental Earth Sciences, 78, 662, doi:10.1007/s12665-019-8670-9, 2019.

Stevanović, Z., Gunn, J., Goldscheider, N., and Ravbar, N.: Karst: Environment and Management of Aquifers. The
870 Groundwater Project. https://doi.org/10.62592/AWCU2984, 2024.

Tobin, B. W. and Schwartz, B. F.: Quantifying the role of karstic groundwater in a snowmelt-dominated hydrologic system. Hydrological Processes, 34, 3439–3447, doi:10.1002/hyp.13833, 2020.

Toop, D. C., and de la Cruz, N. N.: Hydrogeology of the Canmore Corridor and Northwestern Kananaskis Country, Alberta. Alberta Environment, Hydrogeology Section, 2002.

875 U.S. Environmental Protection Agency (USEPA): The Qtracer2 program for tracer-breakthrough curve analysis for tracer tests. In: Karstic aquifers and other hydrologic systems. U.S. Environmental Protection Agency, Office of Research and Development, National Center for Environmental Assessment, Washington Office, Washington, DC, EPA/600/R-02/001, 2002.

Virtanen, P., Gommers, R., Oliphant, T. E., Haberl, M., Reddy, T., Cournapeau, D., … SciPy 1.0 Contributors: SciPy 1.0:
880 Fundamental algorithms for scientific computing in Python. Nature Methods, 17, 261–272. doi:10.1038/s41592-019-0686-2, 2020.

Western Canada Bryophyte and Lichen Research Group (WCBLIG): Kananaskis Country Watridge Karst Springs, https://wcblig.com (last access: 30 May 2025), 2015.

Werner, E.: Alpine karst in the Rocky Mountains - Introduction to the symposium. National Speleological Society Bulletin,
885 41, 51–52, 1979.

Worthington, S.: Karst hydrogeology of the Canadian Rocky Mountains. Ph.D. Thesis, McMaster University, http://hdl.hle.net/11375/8329, 1991.

Worthington, S. R. H.: How preferential flow delivers pre-event groundwater rapidly to streams. Hydrological Processes, 33, 2373–2380. doi:10.1002/hyp.13520, 2019.

890 Worthington, S.R.H., Davies, G. J., and Alexer, E. C.: Enhancement of bedrock permeability by weathering. Earth-Science Reviews, 160, 188–202. doi:10.1016/j.earscirev.2016.07.002, 2016.

Worthington, S. and Soley, R.: Identifying turbulent flow in carbonate aquifers. Journal of Hydrology, 552, 70–80, doi:10.1016/j.jhydrol.2017.06.045, 2017.

Worthington, S. R. H. and Foley, A. E.: Deriving celerity from monitoring data in carbonate aquifers. Journal of Hydrology,
895 598, 126451, doi:10.1016/j.jhydrol.2021.126451, 2021.

Yonge, C. J., and Lowe, D. J.: Hydrogeology of the Banff Hot Springs, Banff National Park, Canada: a karst perspective. Cave and Karst Science, 44, 82–93, 2017.